

Mapping the star formation history of Mrk 86^{*}

I. Data and models

A. Gil de Paz¹, J. Zamorano¹, J. Gallego¹, and F. de B. Domínguez²

¹ Departamento de Astrofísica, Universidad Complutense de Madrid, Avda. Complutense s/n, E-28040 Madrid, Spain

² OTRI, Universidad Carlos III de Madrid, C/ Butarque, 15, E-28911 Leganés, Spain

e-mail: gil@astrax.fis.ucm.es (AGdP)

Received November 23, 1999; accepted June 8, 2000

Abstract. We have obtained optical (BVR , $[O\text{III}]\lambda 5007\text{ \AA}$ and $H\alpha$), near infrared (JHK) imaging and long-slit optical spectroscopy for the Blue Compact Dwarf galaxy Mrk 86 (NGC 2537). In this paper, the first of two, we present optical-near-infrared colors and emission-line fluxes for the currently star-forming regions, intermediate aged starburst and underlying stellar population. We also describe the evolutionary synthesis models used in Paper II.

The R and $H\alpha$ luminosity distributions of the galaxy star-forming regions show maxima at $M_R = -9.5^m$ and $L_{H\alpha} = 10^{37.3} \text{ erg s}^{-1}$. The underlying stellar population shows an exponential surface brightness profile with central value, $\mu_{E,0} = 21.5 \text{ mag arcsec}^{-2}$, and scale, $\alpha = 0.88 \text{ kpc}$, both measured in the R -band image. In the galaxy outer regions, dominated by this component, no significant color gradients are observed.

Finally, a complete set of evolutionary synthesis models have been developed, covering a wide range in metallicity, $1/50 Z_{\odot} < Z < 2 Z_{\odot}$, and burst strength, $1 - 10^{-4}$. These models include nebular continuum and recombination and forbidden-line emission.

Key words: individual: Mrk 86 — galaxies: irregular, star clusters, stellar content

1. Introduction

The high star formation rate (SFR hereafter) and low neutral gas content deduced for dwarf star-forming galaxies imply consumption time-scales of about 10^9 yr (Fanelli et al. 1988; Thuan & Martin 1981), much shorter than the age of the Universe. Searle et al. (1973) suggested that either these objects are truly young systems or they have an intermittent star formation history with short intense star-forming episodes followed by long quiescent phases. Although this question remained unanswered during decades (Thuan 1983; Campbell & Terlevich 1984; Loose & Thuan 1985), nowadays, most of the studies on dwarf star-forming systems, including Blue Compact Dwarf galaxies (BCD hereafter), have revealed the existence of an evolved underlying population (Kunth et al. 1988; Hoffman et al. 1990; Papaderos et al. 1996b; Doublier 1998; Norton & Salzer 1997).

Therefore, the understanding of the mechanism, or mechanisms, governing this star formation regulation is the stepping stone of the dwarf star-forming galaxies evolution. Moreover, this mechanism constitutes the missing link between the different dwarf star-forming galaxies (Silk et al. 1987; Burkert 1989; Drinkwater & Hardy 1991; Papaderos et al. 1996b).

There are two different approaches to address these questions. On the one hand, statistical analysis of a sample of these objects will allow the study of the relationships between fundamental parameters and properties of the star-forming dwarf galaxies (Marlowe et al. 1995; Papaderos et al. 1996a, 1996b). On the other hand, the detailed analysis of individual low-redshift objects with multiple regions of star formation is fundamental to reconstruct their star formation histories. In particular, we can obtain a better understanding of possible effects of merging or some internal process as self-propagation that could originate the spreading of star formation, and the effects of these star-forming events on the future star formation.

Send offprint requests to: A. Gil de Paz

^{*} Visiting Astronomer (AGdP), Kitt Peak National Observatory, National Optical Astronomy Observatories, which is operated by the Association of Universities for Research in Astronomy, Inc. (AURA) under cooperative agreement with the National Science Foundation.

Among dwarf galaxies, Blue Compact Dwarf galaxies conform the subpopulation where the star-forming events are most violent. Blue Compact Dwarfs are low-luminosity ($M_B \geq -18^m$)¹ galaxies with compact sizes whose spectra are similar to those of low metallicity H II regions (Searle & Sargent 1972; Kunth & Sargent 1986; Thuan & Martin 1981). Their spectra are characterized by emission lines over a blue continuum which implies the existence of a large fraction of OB stars and an intense star-forming activity.

The Blue Compact Galaxy Mrk 86 = NGC 2537 (Shapley & Ames 1932; Markarian 1969), also known as Arp 6 (Arp 1966), constitutes an excellent laboratory to test the BCD star formation history since its star-forming regions populate all the galaxy. This object is the prototype of the iE galaxies, the most important BCD galaxies subclass, that conform 70 per cent of the BCD galaxies (Thuan & Martin 1981; Thuan 1991).

Optical imaging (both broad- and narrow-band) and near infrared images have been obtained to map the different regions and get insight into the star formation history of every region. In addition, we have obtained very high quality spectra with spatial resolution. The spectra of 22 star-forming knots and of free interim were taken with 10 distinct slit positions and orientations and moderate and high spectral resolution.

After briefly introduce the previous results on Mrk 86 in Sect. 2, we will describe the observations and data reduction in Sect. 3. The data analysis is presented in Sect. 4. We describe the evolutionary synthesis models in Sect. 5. In Sect. 6 we give some results. Finally, our conclusions are presented in Sect. 7.

In Gil de Paz et al. (2000a; Paper II hereafter) we derive the physical properties of the star-forming regions and stellar populations of Mrk 86 comparing our photometric data with the evolutionary synthesis models presented in this paper. Electron densities and temperatures and chemical abundances of the ionized gas in the galaxy star-forming regions will be also obtained. Finally, a global interpretation of the galaxy will be given.

2. Mrk 86

Mrk 86 ($\alpha(2000) = 08^h13^m14.56^s$ $\delta(2000) = +45^\circ59'30.2''$)² is a well-known object among BCD galaxies (Loose & Thuan 1985; Sage et al. 1992; see Table 1). In the Loose & Thuan (1985) BCD classification, Mrk 86 belongs to the iE class: smooth elliptical Low Surface Brightness (LSB) underlying stellar component on which several knots of star formation are superimposed. The present star formation activity is spread out in several clumps over a relatively large fraction

¹ For $H_0 = 75 \text{ km s}^{-1} \text{ Mpc}^{-1}$ (Thuan & Martin 1981).

² Center of the outer isophotes as measured in the R -band (see Sect. 4.1).

Table 1. Collection of the published parameters of Mrk 86

Parameter	Data	Reference
v_\odot	447 km s ⁻¹	(1)
v_{LG}	522 km s ⁻¹	(1)
v_{LG}	460 km s ⁻¹	(2)
Distance	6.9 Mpc	(3)
B	12.8	(4)
$f(1510 \text{ \AA})$	$0.87 \cdot 10^{-14} \text{ erg m}^{-2} \text{ s}^{-1} \text{ \AA}^{-1}$	(5)
$S(2.8 \text{ cm})$	$7 \pm 2 \text{ mJy}$	(6)
$S(6.3 \text{ cm})$	$18 \pm 4 \text{ mJy}$	(7)
$S(1.2 \text{ cm})$	$11 \pm 4 \text{ mJy}$	(7)
$f(12 \text{ } \mu\text{m})$	0.25 Jy	(8)
$f(25 \text{ } \mu\text{m})$	0.42 Jy	(8)
$f(60 \text{ } \mu\text{m})$	3.15 Jy	(8)
$f(100 \text{ } \mu\text{m})$	6.26 Jy	(8)
L_{IR}	$0.35 \cdot 10^9 L_\odot$	(8)
J	13.25	(9)
H	12.57	(9)
K	12.37	(9)
L	12.63	(9)
$M(\text{H I})$	$2.4 \cdot 10^8 M_\odot$	(10)
M_{T}	$5.8 \cdot 10^8 M_\odot$	(10)
$f(\text{H I } 21 \text{ cm})$	2.1 Jy km s^{-1}	(11)
$FWHM_{\text{H I}}$	93 km s^{-1}	(11)
I_{CO}	$0.83 \pm 0.12 \text{ K km s}^{-1}$	(12)

(1) Bottinelli et al. (1990); (2) Rood & Dickel (1976); (3) Sharina et al. (1999); (4) Dultzin-Hacyan et al. (1990); (5) Fanelli et al. (1988); (6) Klein et al. (1991); (7) Klein et al. (1984); (8) Thronson & Telesco (1986); (9) Thuan (1983, measured with 7'' apertures); (10) Thuan & Martin (1981); (11) Verter (1985); (12) Sage et al. (1992).

of its entire surface. In fact, Mrk 86 shows the highest ratio of the area covered by star-forming regions to the total projected area of the galaxy within the sample of Papaderos et al. (1996a).

To this moment Mrk 86 has not been the subject of a single and proof study, inasmuch the large number of published data on it. A collection of the published data is given in Table 1. A more detailed description of the previous observations is given by Gil de Paz et al. (1999; GZG hereafter).

2.1. Distance

Mrk 86 is a nearby star-forming galaxy. The heliocentric recession velocity is $v_\odot = 447 \text{ km s}^{-1}$ (see recession velocities referred to the Local Group in Table 1).

Using the mean blue magnitude of the three brightest blue stars Sharina et al. (1999) derived a distance for this object of 6.9 Mpc with an uncertainty of 20 per cent (Sharina, private communication). We can also estimate the distance to Mrk 86 if we assume that it is gravitationally bounded to the edge-on spiral galaxy UGC 4278 (see Paper II). UGC 4278 has a corrected I -band absolute magnitude of -18.21 ± 0.11 (see Giovanelli et al. 1997)

with a logarithmic 21 cm line width of 2.220 ± 0.019 (in km s^{-1}). Therefore, with respect to the Giovanelli et al. (1997) Tully-Fisher template, this galaxy shows an offset of 0.66^m , which corresponds to a peculiar radial velocity of -253 km s^{-1} . Thus, its recession velocity in the CMB reference frame should be 968 km s^{-1} ($v_{\odot} = 565 \text{ km s}^{-1}$), which implies a minimum distance for Mrk 86 of 13 Mpc (for $H_0 = 75 \text{ km s}^{-1} \text{ Mpc}^{-1}$ and assuming that the difference in heliocentric velocity is due to orbital motion). The large difference between this value and that given by Sharina et al. (1999) suggests that these objects are probably not physically bounded. Thus, since no other distance indicator is available for Mrk 86, we have used the distance measured by Sharina et al. (1999) throughout this work. This value leads a projected spatial scale of $33 \text{ pc arcsec}^{-1}$.

3. Observations and reduction

3.1. Optical imaging

An optical *B*-band image was obtained at the 1-m Jacobus Kapteyn Telescope (JKT) of Roque de los Muchachos observatory (La Palma, Spain) in 1997 November with a $24 \mu\text{m}$ 1024×1024 pixels Tek#4 CCD (see Table 2). An additional Johnson-*V* image was taken at the 1.52-m spanish telescope at EOCA (Calar Alto, Almería, Spain) in December 1993 with a Tek 1024×1024 CCD with pixel size of $19 \mu\text{m}$. This observation was broken up into five exposures with a total integration time of 2400 s. Finally, an *R*-band image was obtained during service time in November 1998 with the ING wide-field camera (ING-WFC) equipped with four EEV42 $2k \times 4k$ pixels CCD detectors on the 2.5-m Isaac Newton Telescope (La Palma, Spain).

Narrow-band images in the light of $[\text{O III}]\lambda 5007 \text{ \AA}$ ($\lambda_0 = 5012 \text{ \AA}$, $FWHM = 50 \text{ \AA}$) and $\text{H}\alpha$ ($\lambda_0 = 6568 \text{ \AA}$, $FWHM = 95 \text{ \AA}$) were obtained. In order to subtract the continuum, *V* and *R*-band images were used, respectively. The $[\text{O III}]\lambda 5007 \text{ \AA}$ image was secured for us on December 1993 during service time with a 1280×1180 pixels EEV5 CCD attached to the 2.5-m Isaac Newton Telescope. The $\text{H}\alpha$ image was taken during the same service time observations that the *R*-band image in November 1998 using the ING-WFC camera at the 2.5-m Isaac Newton Telescope (La Palma, Spain).

High S/N ratio dome flats and exposures of the sky taken in twilight were obtained in any case. The standard procedure of bias removal, dark-current subtraction, and flat fielding using dome and sky flat-field images was performed using the ESO image processing system MIDAS for the *V* image and IRAF³ for the *B* and *R*-band images.

³ IRAF is distributed by the National Optical Astronomy Observatories, which are operated by the Association of Universities for Research in Astronomy, Inc., under cooperative agreement with the National Science Foundation.

Table 2. Journal of observations

Spectroscopic Observations [†]				
Telescope	Exp. time(s)	Slit	Range (nm)	Disp. ($\text{\AA}/\text{pix}$)
CAHA 2.2 m	3600	#1,2,4,6 <i>b</i>	330 – 580	2.6
CAHA 2.2 m	1800	#5 <i>b</i>	330 – 580	2.6
CAHA 2.2 m	3600	#1,2,4,5,6 <i>r</i>	435 – 704	2.6
CAHA 2.2 m	3600	#3	390 – 650	2.6
INT 2.5 m	1800	#7,8 <i>R</i>	637 – 677	0.39
INT 2.5 m	900	#9 <i>R</i>	637 – 677	0.39
Image Observations				
Telescope	Exp. time(s)	Filter	Scale ($''/\text{pixel}$)	PSF ($''$)
JKT 1.0 m	600	<i>B</i>	$0''.33$	$1''.0$
CAHA 1.5 m	2400	<i>V</i>	$0''.33$	$1''.6$
INT 2.5 m	900	<i>R</i>	$0''.333$	$1''.2$
INT 2.5 m	900	$[\text{O III}]\lambda 5007$	$0''.57$	$2''.5$
INT 2.5 m	7200	$\text{H}\alpha$	$0''.333$	$1''.2$
KPNO 2.3 m	900	<i>J</i>	$0''.66$	$1''.8$
KPNO 2.3 m	360	<i>H</i>	$0''.66$	$1''.6$
KPNO 2.3 m	540	<i>K</i>	$0''.66$	$1''.7$

[†] See Fig. 1 of GZG for slit orientations and positions.

Atmospheric conditions were photometric during the observing runs. *B* and *V* images were flux calibrated observing repeatedly during the nights a set of standard stars, taken from the lists given by Kent (1985) and Landolt (1973). Finally, the *R*-band image was flux calibrated using the radial surface brightness profile published by Papaderos et al. (1996a).

The $[\text{O III}]\lambda 5007 \text{ \AA}$ and $\text{H}\alpha$ images flux calibration was performed as follows (see also GZG). The continuum emission was subtracted, using the *V* and *R* images, respectively. Then, we trimmed those regions covered by the slits of the *b*(blue) and *r*(red) spectra (see Table 2). The *b* and *r* spectra were convolved with the transmission curves of the corresponding narrow-band filters. Then, we compared image counts and fluxes measured in the convolved spectra for several adjacent regions in order to determine the precise location of the slits. Finally, once the regions covered by the slits were precisely defined, we corrected these calibration relations for the sensitivity of the filter at the corresponding wavelength and, in the case of the $\text{H}\alpha$ flux, for the contribution of the $[\text{N II}]\lambda 6548 \text{ \AA}$ and $[\text{N II}]\lambda 6583 \text{ \AA}$ lines. The discrepancies obtained among different spectra were in all cases lower than 10 per cent.

3.2. Near-infrared imaging

Near-infrared images (nIR hereafter) of Mrk 86 in *J* ($\lambda_0 = 1.25 \mu\text{m}$, $FWHM = 0.30 \mu\text{m}$), *H* ($\lambda_0 = 1.65 \mu\text{m}$, $FWHM = 0.28 \mu\text{m}$) and *Ks* ($\lambda_0 = 2.15 \mu\text{m}$, $FWHM = 0.33 \mu\text{m}$) were obtained on January 1998 with the Steward Observatory near-infrared camera equipped with a 256×256 NICMOS3 detector attached to the 2.3-m Bok Telescope at Kitt Peak National Observatory (Arizona, U.S.A.). The observational procedure closely

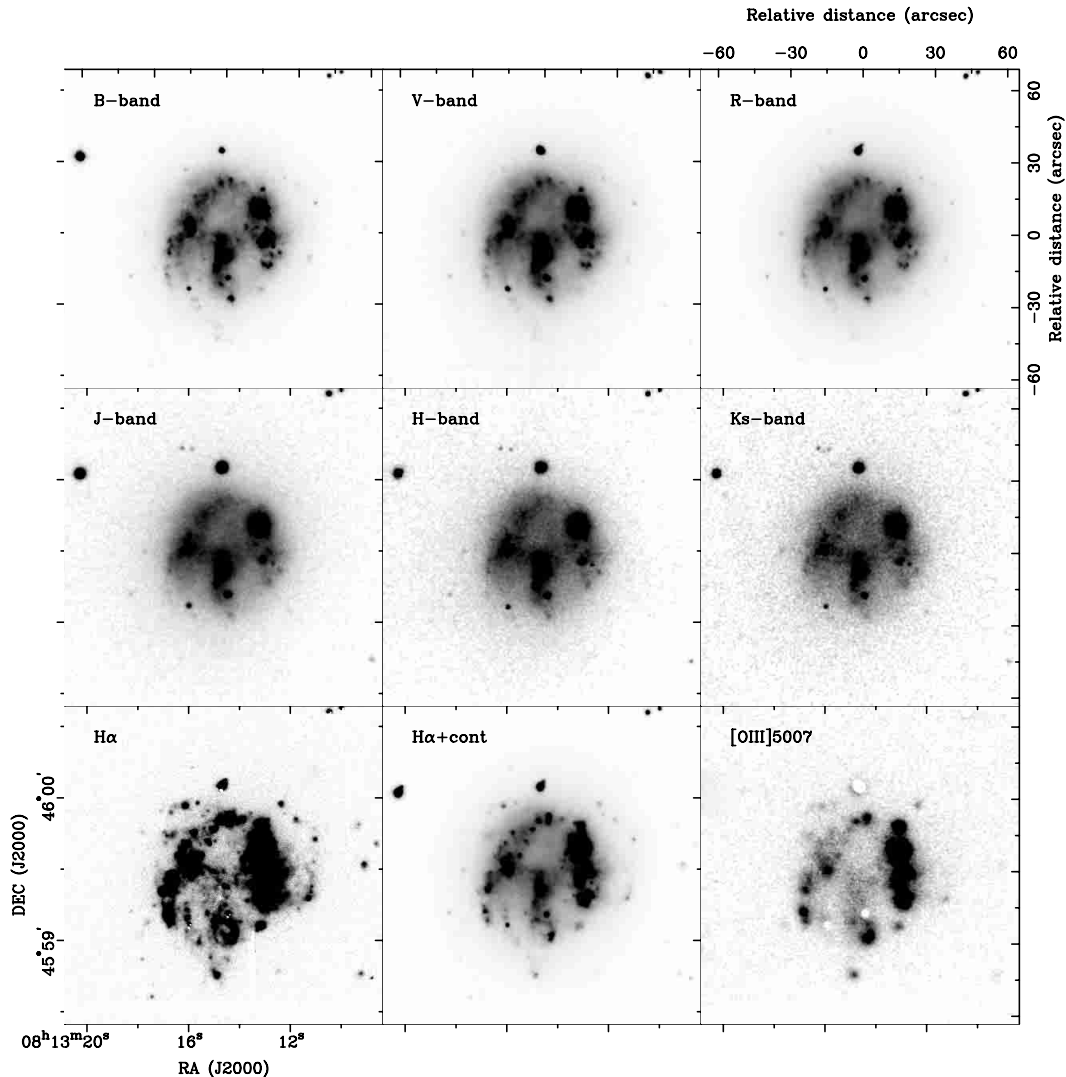


Fig. 1. *BVRJHK*, $H\alpha$ and $[O\text{ III}]\lambda 5007\text{ \AA}$ images of Mrk 86

follows that of Aragón-Salamanca et al. (1993) and Gil de Paz et al. (2000b). The total integration time of each subimage was broken up into background-limited sub-exposures to avoid saturation of the detector. Images of adjacent blank areas of the sky were alternated with the target frames for accurate flat-fielding. Comparable amounts of time were spent imaging the source and the sky to ensure adequate monitoring of the sky changes. Individual subexposures of the object were offset several arcseconds to improve the final result.

The reduction process include: (1) bias and dark subtraction of object and sky frames; (2) flat-fielding using normalized sky frames; (3) sky subtraction using sky frames taken before and after each exposure; (4) bad pixel removal; (5) registering of the subimages using fractional pixel shifts and (6) median combining of all individual frames. The reduction was carried out using own IRAF procedures.

The nIR images were calibrated observing standard stars from the list from Elias et al. (1982) during the nights

at the same airmasses than the object. We have assumed a color independent correction between the Ks and K' bands ($K' \equiv KM$; $\lambda_0 = 2.12\text{ }\mu\text{m}$, $FWHM = 0.34\text{ }\mu\text{m}$; Wainscoat & Cowie 1992). In order to check the validity of this assumption, we convolved the Ks and K' filters response functions with Planck spectral distributions at different temperatures in the range 3000 – 20000 K, obtaining the fluxes F_{Ks} and $F_{K'}$. The larger difference in $2.5 \times \log(F_{Ks}/F_{K'})$ within this temperature range was 0.025^m , small enough to assume this correction to be independent of the spectral energy distribution.

Thus, once the fluxes were transformed to K' -band fluxes, we converted them to the standard K -band ($\lambda_0 = 2.19\text{ }\mu\text{m}$, $FWHM = 0.41\text{ }\mu\text{m}$) applying the standard correction given by Wainscoat & Cowie (1992), $K' - K = 0.22 \times (H - K)$.

In Fig. 1 we show the Mrk 86 neighborhood in the optical-near-infrared bands studied, including the $H\alpha$ and $[O\text{ III}]\lambda 5007\text{ \AA}$ images. The astrometric calibration was performed using the program

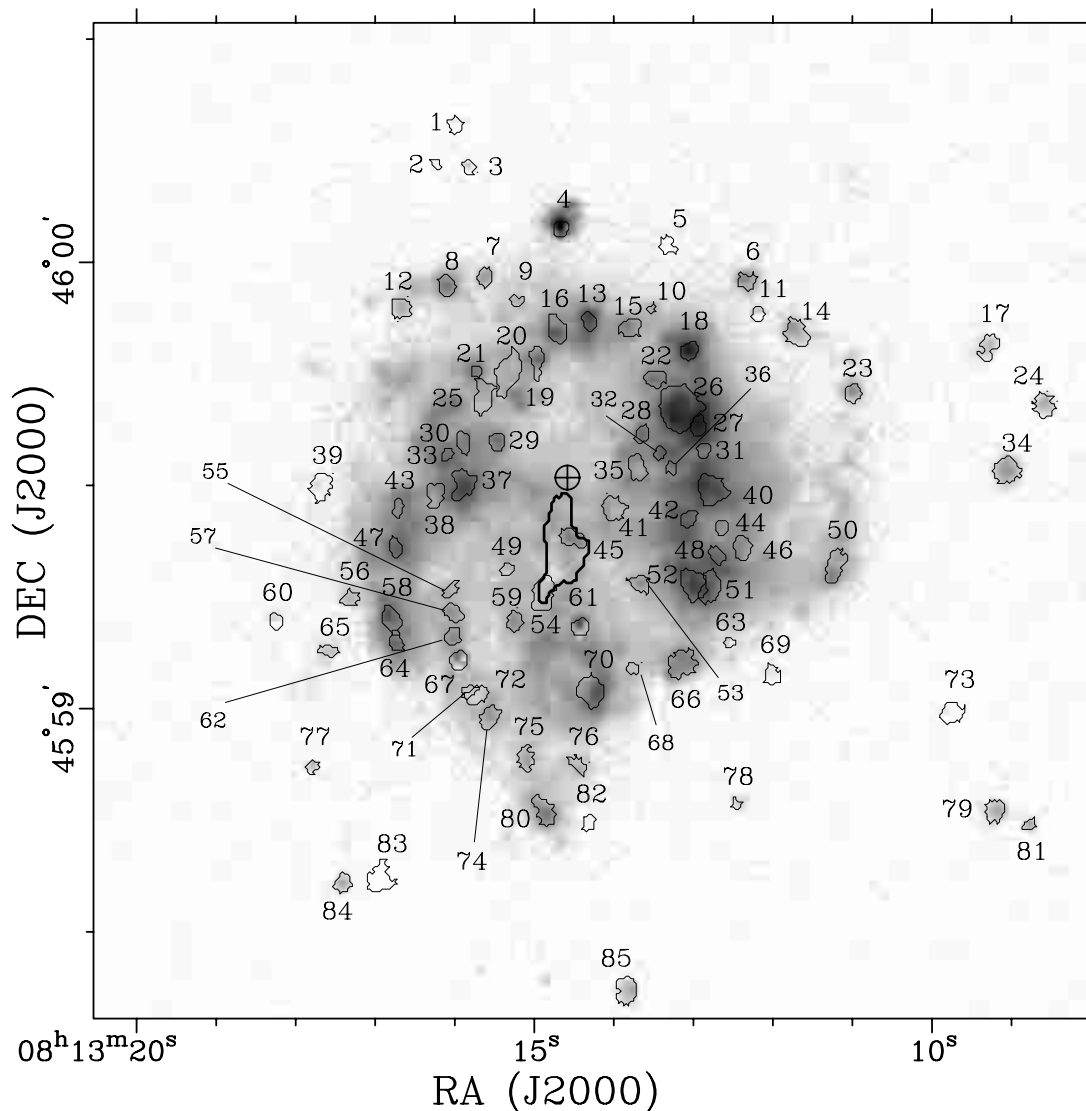


Fig. 2. Knot contours derived using the COBRA program superimposed on the $H\alpha$ image. The *thick-lined* contour corresponds to the starburst component as described by Papaderos et al. (1996a, see Sect. 6.3). The crossed-circle position marks the center of the outer R -band isophotes

PLATEASTROM (García-Dabó & Gallego 1999; see also <http://www.ucm.es/info/Astrof/opera/opera.html>). The bright field star placed at the relative position ($60''$ E, $30''$ N), saturated in the V and R -band images, was artificially removed.

3.3. Spectroscopy

Up to 14 optical long-slit spectra at 10 different slit positions were obtained. The 11 medium-low resolution spectra (b and r spectra; see Table 2) were obtained with the Boller & Chivens spectrograph at the Cassegrain focus of the 2.2-m telescope at the German-Spanish Calar Alto observatory (Almería, Spain) in January 1993. Although special care was taken to place the slits into position, using offsets from the bright field

star at north of the galaxy, there were some lack of precision. The actual positions of the slits (see Fig. 1 of GZG) were determined a posteriori comparing broadband image spatial cuts with the spatial profiles of the spectra previously convolved with the corresponding filter transmission curves. The detector employed was a 1024×1024 Tek#6 CCD with a pixel size of $24 \mu\text{m}$. The 600 gr mm^{-1} grating chosen provided a spectral resolution of 6 \AA in the light of $H\alpha$ and a reciprocal dispersion of 2.6 \AA/pixel , with a slit width of $2''.65$. The final spatial scale was $1''.43/\text{pixel}$. The spectral coverage was around 2500 \AA and the grating angle was selected to cover the blue region ($\sim 3300 - 5800 \text{ \AA}$) and red domain ($\sim 4350 - 7045 \text{ \AA}$) in two different exposures which overlapped on the $H\beta$ region. The seeing was variable during the observing run with $FWHM$ between $1''.5 - 2''.5$. The low airmasses at which these spectra were obtained

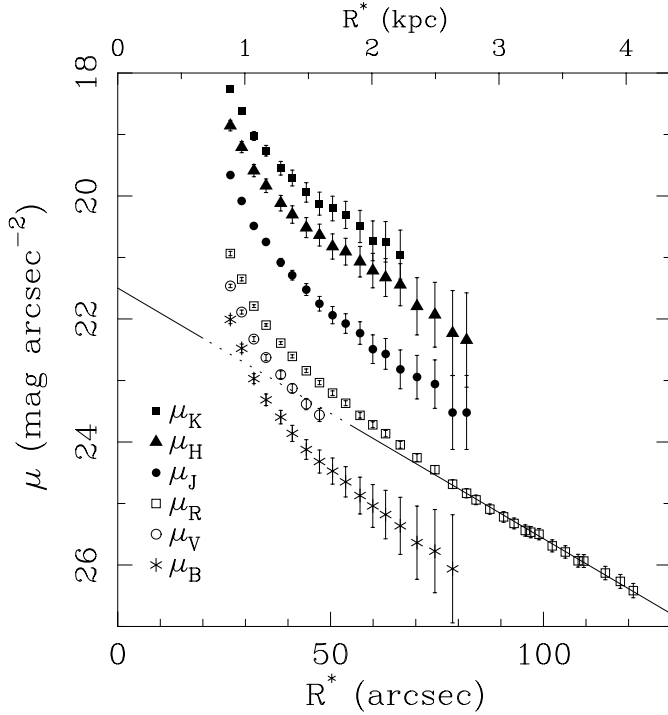


Fig. 3. Surface brightness profiles in the *BVRJHK* bands. The fit to the exponential component of the *R*-band profile at distances larger than $70''$ is also drawn. Error bars represent $\pm 1\sigma$. The *K*-band profile has been offset -0.5^m in order to avoid confusion with the *H*-band profile

(≤ 1.2) guarantee that no significant loss of blue light due to atmospheric refraction has occurred. In addition, three high resolution spectra (7R, 8R, 9R) were obtained with the IDS spectrograph at the Isaac Newton Telescope (INT) of the Roque de los Muchachos Observatory (La Palma, Spain) in January 1998 with a 1024×1024 Tek#3 $24 \mu\text{m}$ CCD (see Table 2). The 1200R grating (1200 gr mm^{-1}) was used with an slit width of $1''$, providing a spectral resolution of 0.9 \AA in the light of $\text{H}\alpha$ and a reciprocal dispersion of 0.39 \AA/pixel . The spatial scale was of $0.33''/\text{pixel}$.

These spectra were reduced using the FIGARO (January 1993) and IRAF (January 1998) software packages. After bias removal and flat-fielding, the frames were cleaned of cosmic rays. The sky was removed from each frame by subtracting a polynomial fitted to those regions free for object emission. Wavelength calibration was performed by using He-Ar lamps observed immediately before and after the galaxy integration. The standard stars Hiltner 102 and Hiltner 600 were observed at different airmasses in order to correct for atmospheric extinction and to ensure absolute flux calibration.

Finally, we requested an UV spectrum of Mrk 86 from the International Ultraviolet Explorer (IUE) Final Archive (see Fig. 4). It was originally taken by Alloin and Duflot in January 1983 (see Bonatto et al. 1999). The total exposure time of this spectrum, SWP18927, was 24000 s. It was

Table 3. Positions and sizes for the Mrk 86 neighborhood regions

#	#'	RA(2000)	DEC(2000)	r_{1e}	r'_{1e}	e	Cl.
(1)	(2)	(3)	(4)	(5)	(6)	(7)	(8)
01	–	08:13:16.08	+46:00:17.1	0.71	PLR	2	B
02	–	08:13:16.33	+46:00:12.1	0.85	0.45	1	B
03	–	08:13:15.91	+46:00:11.8	0.74	0.17	2	B
04	01	08:13:14.72	+46:00:04.1	1.13	0.87	2	F
05	–	08:13:13.38	+46:00:01.7	0.91	0.56	2	B
06	02	08:13:12.36	+45:59:57.6	1.07	0.79	2	E
07	–	08:13:15.70	+45:59:57.4	0.83	0.41	2	E
08	03	08:13:16.18	+45:59:56.0	0.96	0.63	2	E
09 [†]	–	08:13:15.28	+45:59:54.1	0.76	0.24	2	E
10 [†]	–	08:13:13.56	+45:59:53.4	0.68	PLR	1	E
11	04	08:13:12.20	+45:59:53.0	0.75	0.21	2	B
12 [†]	–	08:13:16.74	+45:59:52.9	1.06	0.78	2	E
13	05	08:13:14.36	+45:59:52.0	1.31	1.09	1	E
14	06	08:13:11.72	+45:59:50.7	1.36	1.15	2	S
15	08	08:13:13.85	+45:59:50.7	0.96	0.63	2	E
16	07	08:13:14.77	+45:59:50.6	1.72	1.56	1	S
17	–	08:13:09.23	+45:59:49.5	1.03	0.74	2	E
18	09	08:13:13.08	+45:59:48.2	0.93	0.59	2	S
19	10	08:13:15.02	+45:59:45.3	1.56	1.38	1	S
20	11	08:13:15.33	+45:59:45.2	2.29	2.17	1	S
21	12	08:13:15.78	+45:59:44.8	0.88	0.51	1	E
22 [†]	13	08:13:13.52	+45:59:44.2	1.02	0.72	2	E
23	14	08:13:10.94	+45:59:43.0	0.97	0.65	2	E
24	–	08:13:08.52	+45:59:41.4	1.19	0.95	2	E
25	–	08:13:15.64	+45:59:41.2	1.39	1.19	2	N
26	15	08:13:13.13	+45:59:40.6	2.11	1.98	2	S
27	16	08:13:12.94	+45:59:38.4	1.32	1.11	1	S
28 [†]	17	08:13:13.64	+45:59:36.9	0.84	0.43	2	E
29	18	08:13:15.51	+45:59:35.6	0.85	0.45	2	S
30	19	08:13:15.92	+45:59:35.6	0.93	0.59	2	E
31	20	08:13:12.87	+45:59:35.1	0.65	PLR	2	N
32	21	08:13:13.41	+45:59:34.3	0.69	PLR	2	S
33	22	08:13:16.11	+45:59:33.9	0.96	0.63	1	E
34	–	08:13:08.99	+45:59:33.0	1.32	1.11	2	E
35	23	08:13:13.69	+45:59:33.0	1.28	1.06	2	N
36	24	08:13:13.28	+45:59:32.4	0.71	PLR	2	N
37	26	08:13:15.88	+45:59:29.3	1.90	1.76	1	S
38	27	08:13:16.23	+45:59:29.2	0.94	0.60	2	N
39	28	08:13:17.76	+45:59:29.0	1.20	0.96	2	B
40	25	08:13:12.76	+45:59:28.8	1.62	1.45	2	S
41	29	08:13:14.04	+45:59:27.3	1.07	0.79	2	S
42	31	08:13:12.98	+45:59:26.5	1.29	1.07	1	S
43	32	08:13:16.77	+45:59:25.9	1.12	0.86	1	E
44	33	08:13:12.63	+45:59:24.6	0.79	0.33	2	N
45	–	08:13:14.57	+45:59:23.2	1.15	0.90	2	S
46	34	08:13:12.37	+45:59:22.3	1.03	0.74	2	N
47	36	08:13:16.76	+45:59:21.2	1.22	0.98	1	S
48	35	08:13:12.69	+45:59:21.2	1.18	0.93	1	E
49	–	08:13:15.36	+45:59:18.8	0.73	0.12	2	N
50	37	08:13:11.19	+45:59:18.8	1.42	1.22	2	E
51	38	08:13:12.72	+45:59:17.3	1.28	1.06	2	N
52	39	08:13:12.97	+45:59:17.2	1.32	1.11	2	S
53 [†]	–	08:13:13.64	+45:59:17.1	0.86	0.47	2	E
54	40	08:13:14.91	+45:59:15.9	2.01	1.88	1	S
55 [†]	–	08:13:16.12	+45:59:15.8	0.69	PLR	2	E
56	–	08:13:17.35	+45:59:14.6	0.81	0.37	2	E

Table 3. continued

#	#'	RA(2000)	DEC(2000)	r_{1e}	r'_{1e}	e	Cl.
(1)	(2)	(3)	(4)	(5)	(6)	(7)	(8)
57 [†]	–	08:13:16.05	+45:59:13.1	0.82	0.39	2	E
58	41	08:13:16.84	+45:59:12.3	1.00	0.69	2	E
59	44	08:13:15.25	+45:59:11.6	0.86	0.47	2	S
60	43	08:13:18.27	+45:59:11.4	0.86	0.47	2	E
61	42	08:13:14.39	+45:59:11.4	0.77	0.27	3	F
62	–	08:13:16.04	+45:59:09.8	1.28	1.06	1	S
63	–	08:13:12.48	+45:59:09.4	0.56	PLR	2	N
64	45	08:13:16.74	+45:59:08.7	1.30	1.08	1	E
65	–	08:13:17.60	+45:59:07.6	1.22	0.98	1	E
66	46	08:13:13.05	+45:59:07.0	1.47	1.28	2	S
67	47	08:13:15.94	+45:59:06.9	0.80	0.35	3	F
68	–	08:13:13.75	+45:59:05.9	0.62	PLR	2	E
69	48	08:13:11.94	+45:59:05.2	0.95	0.62	2	B
70	49	08:13:14.28	+45:59:02.8	1.43	1.24	2	S
71	–	08:13:15.81	+45:59:02.6	0.75	0.21	2	N
72	50	08:13:15.68	+45:59:02.0	1.05	0.76	2	N
73	–	08:13:09.67	+45:59:00.6	1.08	0.80	2	B
74	–	08:13:15.52	+45:58:59.0	1.08	0.80	2	E
75	–	08:13:15.07	+45:58:53.5	0.95	0.62	2	E
76 [†]	–	08:13:14.36	+45:58:52.3	1.11	0.84	1	E
77	–	08:13:17.80	+45:58:52.1	0.87	0.49	2	E
78	–	08:13:12.32	+45:58:48.3	1.03	0.74	1	E
79 [†]	–	08:13:09.05	+45:58:47.9	1.13	0.87	2	E
80	51	08:13:14.77	+45:58:46.0	1.09	0.82	2	E
81 [†]	–	08:13:08.64	+45:58:46.0	0.64	PLR	2	B
82	–	08:13:14.26	+45:58:45.1	0.85	0.45	2	B
83	–	08:13:16.92	+45:58:37.0	1.25	1.02	2	B
84 [†]	–	08:13:17.39	+45:58:36.6	0.91	0.56	2	E
85	55	08:13:13.69	+45:58:23.4	1.37	1.17	2	S

- (1) Knot number (reverse DEC sorted).
(2) Old knot number as given in GZG.
(3) RA(J2000).
(4) DEC(J2000).
(5) Radius (in arcsec) at 1e-folding.
(6) Radius (in arcsec) corrected for the atmospheric seeing.
(7) Folding (e^1 , e^2 or e^3) where colors were measured.
(8) Classification (see Sect. 4.3).
PLR = Point-Like Region.
[†] Knot sizes measured on the H α image (see Sect. 4.2).

obtained in low dispersion mode with the SWP camera. In the observing spectral range, 1150 – 1975 Å, the resolution power varies between 270 – 300 (Cassatella et al. 1985).

4. Analysis

4.1. Surface brightness profiles

We have analyzed the surface brightness profile of Mrk 86 in different bands (*BVRJHK*; see Fig. 3). These surface brightness profiles have been obtained using the IRAF task ELLIPSE. Background galaxies and foreground stars were interactively masked. We obtained the surface brightness profiles over the original images, excepting in the

outer regions of the *R*-band profile where a median filter of 5×5 pixels ($0''.333/\text{pixel}$) was applied. Due to the contribution of about 60 high surface brightness regions, we only fitted the isophotes with major axis larger than $25''$. Using the mean of the isophotal centers measured between 80 and $120''$ in the *R*-band image we have estimated the galaxy coordinates given in Sect. 2 (see also Fig. 2).

4.2. Knot positions and sizes

In order to derive the positions and sizes of the regions in the neighborhood of Mrk 86 we have developed a program called COBRA (see Appendix). Briefly, this program selects the image section where the region of interest is placed. Then, the light profiles in both image axes are fitted using a straight line, in order to account for the underlying emission, and two Gaussians reproducing the knot emission profile. The center of the knot is estimated as the maximum of this latter component. The positions derived for all these regions are given in Table 3 (Cols. 3 and 4). They have been numbered in reverse declination order. Most of these regions were identified on the Johnson *R*-band image, the deepest of those shown in Fig. 1 (For $R = 25.6$ the signal-to-noise ratio is 30). However, some regions showed intense H α emission, but practically no optical or near-infrared continuum emission (see Table 3). Since more than thirty new objects are identified in this *R*-band image relative to the Gunn-*r* image used in GZG, we have introduced a new notation for the knots. In this sense, the regions numbered as #9, #15, #16, #31 and #49 in GZG, now are, respectively, #18, #26, #27, #42 and #70 (see Fig. 2 and Table 3).

The determination of the boundaries of these knots is not an obvious task.

Some authors simply locate the position of the knots by using a weighted mean of the pixels surrounding a maximum of intensity and then they use large enough circular apertures to perform the photometry. This simple approach assume circular geometry for the knots, a prerequisite which is not always fulfilled. An autonomous feature, commonly an HII region, can be also defined as the region which is inside its outermost closed contour (Petrosian et al. 1997) or selecting all pixel that are connected above a given threshold using predetermined background and noise properties of the frame (Mazzarella et al. 1993). All these methods, reviewed in Fuentes-Masip (1997), are difficult to apply in overcrowded fields or when there is a very intense and variable background emission. We have applied a new method which, using interactively the COBRA code, is able to eliminate the emission of adjacent regions and, specially, the low-frequency contamination. This contamination is quite relevant in this object due to the contribution of the underlying stellar population emission to the surface brightness of the galaxy.

After the underlying emission was subtracted, we estimated the number of pixels above different thresholds

Table 4. Photometric magnitudes, colors and H α fluxes

#	B \ddagger (2)	V (3)	R (4)	J (5)	H (6)	K' (7)	B-V (8)	V-R (9)	R-J (10)	J-H (11)	H-K' (12)	R(km/s) (13)	F(H α) (14)
1	22.54±0.10	21.97±0.07	21.20±0.09	20.09±0.31	19.15±0.21	18.67±0.27	0.57±0.13	0.77±0.12	1.11±0.32	0.94±0.38	0.49±0.34	22.27±0.06	-
2	23.38±0.11	22.72±0.07	21.81±0.10	18.71±0.04	18.16±0.09	17.79±0.06	0.66±0.13	0.91±0.10	3.11±0.08	0.54±0.10	0.37±0.11	22.315±0.064	-
3	22.55±0.06	21.72±0.05	20.81±0.07	18.59±0.06	17.85±0.09	17.61±0.08	0.89±0.11	0.90±0.11	2.23±0.12	0.74±0.11	0.24±0.13	21.186±0.087	-
4	17.80±0.06	16.38±0.01	18.30±0.01	13.30±0.01	14.33±0.06	12.41±0.01	1.43±0.06	-	-	-	1.04±0.08	15.176±0.257	-
5	21.29±0.07	20.60±0.03	20.01±0.12	18.77±0.11	18.08±0.12	17.79±0.14	0.69±0.07	0.59±0.12	1.24±0.16	0.69±0.16	0.28±0.18	22.013±0.066	0.104E-14±0.410E-16
6	20.87±0.07	20.57±0.03	20.03±0.12	18.96±0.14	18.22±0.13	18.17±0.22	0.65±0.13	0.54±0.13	1.07±0.18	0.74±0.19	0.05±0.26	22.024±0.066	0.396E-15±0.307E-16
7	20.20±0.02	20.20±0.02	19.59±0.13	18.20±0.06	17.45±0.09	17.36±0.09	0.67±0.07	0.61±0.13	1.38±0.14	0.73±0.11	0.09±0.13	20.988±0.095	0.197E-14±0.198E-16
8	20.50±0.07	20.03±0.02	19.43±0.13	18.13±0.07	17.38±0.10	17.33±0.11	0.47±0.07	0.60±0.13	1.30±0.15	0.76±0.12	0.05±0.15	20.988±0.095	0.114E-15±0.290E-17
9	-	-	-	-	-	-	-	-	-	-	-	-	0.875E-16±0.165E-16
10	21.35±0.07	20.63±0.02	20.08±0.12	18.92±0.09	18.32±0.11	18.03±0.12	0.71±0.07	0.57±0.12	1.16±0.15	0.60±0.14	0.28±0.17	20.817±0.097	0.376E-15±0.341E-17
11	21.01±0.07	18.37±0.03	19.72±0.12	18.35±0.11	17.52±0.11	17.36±0.14	0.64±0.08	0.66±0.13	1.37±0.16	0.83±0.15	0.15±0.17	18.716±0.151	0.108E-13±0.254E-15
12	19.09±0.06	18.75±0.01	18.20±0.16	17.19±0.03	16.51±0.08	16.36±0.04	0.33±0.06	0.55±0.16	1.01±0.17	0.69±0.10	0.15±0.09	20.650±0.088	0.650E-15±0.335E-17
13	20.50±0.07	19.95±0.03	19.32±0.14	18.03±0.12	17.54±0.14	17.26±0.14	0.45±0.08	0.68±0.14	1.28±0.17	0.50±0.18	0.28±0.23	21.170±0.101	0.164E-14±0.132E-16
14	20.20±0.06	18.75±0.01	18.17±0.16	16.95±0.03	16.29±0.08	16.12±0.04	0.58±0.17	0.58±0.17	1.22±0.17	0.66±0.09	0.17±0.09	20.652±0.101	0.260E-14±0.126E-15
15	18.39±0.06	18.00±0.01	17.45±0.18	16.36±0.02	15.63±0.08	15.50±0.03	0.39±0.06	0.55±0.18	1.08±0.18	0.73±0.08	0.13±0.09	18.377±0.162	0.413E-15±0.752E-17
16	22.31±0.14	21.88±0.12	21.20±0.09	19.83±0.45	18.85±0.08	18.85±0.08	0.43±0.19	0.68±0.15	1.37±0.45	0.67±0.09	0.25±0.09	18.575±0.156	0.231E-14±0.192E-16
17	18.93±0.06	18.51±0.01	17.94±0.17	16.97±0.02	16.30±0.08	16.05±0.03	0.41±0.06	0.57±0.17	0.97±0.17	0.73±0.09	0.08±0.09	19.581±0.128	0.180E-14±0.250E-16
18	18.66±0.06	18.23±0.01	17.65±0.18	16.50±0.02	15.77±0.08	15.69±0.03	0.44±0.06	0.58±0.18	1.15±0.18	0.73±0.08	0.15±0.09	18.176±0.165	0.148E-14±0.199E-16
19	17.70±0.06	17.23±0.01	16.67±0.20	15.50±0.02	14.77±0.08	14.62±0.03	0.45±0.06	0.58±0.20	1.17±0.20	0.71±0.08	0.08±0.09	20.636±0.101	0.187E-14±0.192E-16
20	19.85±0.06	19.47±0.01	18.89±0.15	17.69±0.02	16.98±0.08	16.89±0.03	0.38±0.06	0.58±0.15	1.21±0.15	0.71±0.08	0.08±0.09	20.376±0.108	0.459E-15±0.858E-16
21	-	-	-	-	-	-	-	-	-	-	-	-	0.386E-15±0.694E-17
22	20.84±0.02	20.38±0.02	20.00±0.12	18.99±0.14	18.28±0.13	18.00±0.18	0.50±0.07	0.35±0.12	1.01±0.18	0.74±0.19	0.25±0.23	20.376±0.108	-
23	22.54±0.18	22.08±0.16	21.83±0.09	20.69±0.08	19.66±1.35	19.66±1.35	0.48±0.24	0.73±0.18	0.64±1.08	0.64±1.08	0.11±0.09	19.850±0.121	-
24	18.02±0.06	17.60±0.01	17.03±0.19	15.88±0.02	15.16±0.08	15.09±0.03	0.43±0.06	0.37±0.19	1.19±0.20	0.72±0.08	0.17±0.08	19.122±0.244	0.299E-13±0.300E-15
25	19.96±0.06	19.49±0.01	14.82±0.45	13.87±0.01	13.15±0.08	12.93±0.02	0.46±0.06	0.37±0.25	1.08±0.25	0.75±0.08	0.17±0.08	16.791±0.201	0.619E-13±0.421E-15
26	18.08±0.06	17.67±0.01	17.05±0.19	16.17±0.01	15.35±0.08	15.14±0.02	0.42±0.06	0.63±0.19	0.88±0.19	0.84±0.08	0.19±0.08	-	0.123E-14±0.350E-16
27	19.23±0.06	18.73±0.01	18.12±0.19	17.01±0.02	16.23±0.08	16.13±0.03	0.50±0.06	0.61±0.17	1.10±0.17	0.78±0.08	0.10±0.09	-	0.160E-14±0.868E-17
28	19.07±0.06	18.55±0.01	18.00±0.17	16.83±0.02	16.07±0.08	15.95±0.03	0.51±0.06	0.56±0.17	1.17±0.17	0.76±0.08	0.10±0.09	-	0.474E-15±0.117E-16
29	18.61±0.06	18.28±0.01	17.78±0.01	16.61±0.02	15.82±0.08	15.75±0.03	0.32±0.06	0.51±0.18	1.16±0.18	0.79±0.08	0.07±0.09	20.257±0.111	0.257E-14±0.253E-16
30	19.27±0.06	18.77±0.01	18.17±0.16	17.10±0.02	16.27±0.08	16.17±0.03	0.50±0.06	0.60±0.17	1.06±0.17	0.84±0.08	0.09±0.09	20.838±0.104	0.221E-14±0.299E-16
31	19.61±0.06	19.14±0.01	18.53±0.16	17.41±0.02	16.66±0.08	16.53±0.03	0.47±0.06	0.61±0.16	1.12±0.16	0.76±0.08	0.13±0.09	22.259±0.077	0.105E-14±0.799E-17
32	19.26±0.06	18.94±0.01	18.41±0.16	17.24±0.02	16.49±0.08	16.40±0.03	0.32±0.06	0.54±0.16	1.17±0.16	0.74±0.08	0.10±0.09	19.709±0.125	-
33	21.63±0.11	21.30±0.10	20.61±0.10	19.48±0.46	18.83±0.38	18.65±0.69	0.33±0.15	0.69±0.15	1.13±0.47	0.67±0.60	0.16±0.79	-	-
34	18.58±0.06	18.12±0.01	17.57±0.18	16.45±0.02	15.68±0.02	15.60±0.03	0.45±0.06	0.55±0.18	1.12±0.16	0.77±0.08	0.07±0.09	20.115±0.114	-
35	19.52±0.06	19.07±0.01	18.51±0.16	17.34±0.02	16.55±0.08	16.43±0.03	0.45±0.06	0.56±0.16	1.17±0.16	0.80±0.08	0.11±0.09	21.346±0.083	0.114E-13±0.784E-16
36	18.43±0.06	17.92±0.01	16.84±0.20	15.76±0.02	14.98±0.08	14.90±0.02	0.38±0.06	0.57±0.20	1.08±0.20	0.78±0.08	0.08±0.08	17.932±0.171	-
37	18.03±0.06	17.48±0.01	17.42±0.18	16.12±0.02	15.35±0.08	15.27±0.02	0.45±0.06	0.56±0.18	1.30±0.18	0.77±0.08	0.09±0.08	19.596±0.128	-
38	20.58±0.07	19.80±0.03	19.15±0.14	17.68±0.08	16.87±0.10	16.58±0.09	0.78±0.07	0.50±0.21	1.47±0.16	0.81±0.12	0.28±0.13	19.983±0.118	0.179E-13±0.696E-15
39	18.14±0.06	17.94±0.01	17.37±0.19	16.21±0.02	15.43±0.08	15.37±0.03	0.53±0.06	0.57±0.19	1.15±0.19	0.79±0.08	0.06±0.09	20.423±0.107	-
40	18.46±0.06	17.95±0.01	17.51±0.18	16.62±0.02	15.83±0.08	15.71±0.02	0.19±0.06	0.44±0.18	0.89±0.18	0.79±0.08	0.12±0.08	17.815±0.174	0.269E-14±0.147E-16
41	19.51±0.06	19.19±0.01	18.66±0.15	17.44±0.03	16.77±0.08	16.67±0.04	0.31±0.06	0.54±0.15	1.21±0.15	0.67±0.09	0.10±0.09	20.044±0.117	0.150E-14±0.280E-16
42	19.06±0.06	18.78±0.01	18.36±0.16	17.31±0.02	16.45±0.08	16.35±0.04	0.28±0.06	0.42±0.16	1.05±0.16	0.86±0.09	0.10±0.09	19.535±0.130	-
43	17.93±0.06	17.50±0.01	16.99±0.20	15.87±0.02	15.11±0.08	15.04±0.02	0.43±0.06	0.51±0.20	1.12±0.20	0.76±0.08	0.07±0.08	0.999E-15±0.214E-16	-
44	18.93±0.06	18.59±0.01	18.06±0.17	16.97±0.03	16.14±0.08	16.05±0.04	0.34±0.06	0.53±0.17	1.09±0.17	0.83±0.09	0.09±0.09	19.566±0.131	-
45	19.28±0.06	19.01±0.01	18.47±0.16	17.42±0.03	16.64±0.08	16.52±0.04	0.26±0.06	0.53±0.16	1.08±0.16	0.77±0.09	0.12±0.09	19.228±0.137	0.620E-14±0.530E-16
46	19.16±0.06	18.87±0.01	18.34±0.16	17.42±0.03	16.62±0.08	16.51±0.04	0.29±0.06	0.53±0.16	0.92±0.16	0.80±0.09	0.11±0.09	19.968±0.118	0.346E-14±0.517E-16
47	20.04±0.06	19.48±0.01	19.01±0.15	17.69±0.03	16.88±0.08	16.81±0.04	0.56±0.06	0.57±0.15	1.21±0.15	0.81±0.09	0.07±0.09	21.300±0.084	-
48	20.26±0.07	19.94±0.03	19.41±0.13	18.56±0.18	17.79±0.13	17.80±0.29	0.32±0.07	0.53±0.14	0.83±0.23	1.07±0.23	-0.31±0.32	20.441±0.115	0.100E-14±0.258E-16
49	18.25±0.06	17.99±0.01	17.44±0.18	16.56±0.03	15.73±0.08	15.59±0.04	0.30±0.06	0.51±0.19	0.88±0.19	0.83±0.09	0.14±0.09	18.620±0.154	-
50	18.06±0.06	17.79±0.01	17.22±0.19	16.37±0.03	15.59±0.08	15.39±0.04	0.27±0.06	0.56±0.19	0.86±0.19	0.77±0.09	0.20±0.09	18.434±0.158	0.144E-13±0.276E-15
51	19.99±0.06	19.40±0.01	18.76±0.15	17.53±0.03	16.68±0.08	16.63±0.05	0.59±0.06	0.64±0.15	1.23±0.15	0.86±0.09	0.03±0.10	18.434±0.158	0.396E-15±0.263E-17
52	17.59±0.06	17.24±0.01	16.72±0.20	15.65±0.02	14.86±0.08	14.79±0.03	0.38±0.06	0.53±0.20	1.07±0.20	0.79±0.08	0.07±0.08	17.703±0.177	-
53	21.21±0.07	20.72±0.03	20.12±0.11	18.91±0.12	17.90±0.11	17.91±0.15	0.49±0.07	0.60±0.12	1.21±0.16	1.01±0.16	-0.01±0.19	-	0.990E-16±0.104E-17
54	19.39±0.06	19.08±0.02	18.54±0.16	17.51±0.06	16.63±0.08	16.59±0.08	0.31±0.06	0.53±0.16	1.04±0.16	0.88±0.11	0.03±0.12	19.845±0.121	0.141E-15±0.390E-17
55	19.63±0.06	19.10±0.01	18.52±0.16	17.36±0.03	16.48±0.08	16.48±0.08	0.53±0.06	0.58±0.16	1.16±0.17	0.87±0.09	0.00±0.10	19.845±0.121	0.842E-15±0.642E-17
56	21.45±0.07	20.75±0.02	20.17±0.11	18.78±0.09	17.78±0.09	18.01±0.14	0.71±0.07	0.58±0.12	1.39±0.14	0.85±0.13	-0.22±0.08	20.069±0.116	0.546E-14±0.160E-15
57	18.45±0.06	17.61±0.01	17.09±0.19	15.90±0.01	15.06±0.08	15.03±0.02	0.84±0.06	0.52±0.19	1.19±0.19	0.80±0.13	0.02±0.08	17.234±0.189	0.575E-15±0.613E-17
58	20.09±0.06	19.56±0.01	19.00±0.14	17.75±0.04	16.94±0.09	16.94±0.07	0.53±0.06	0.56±0.14	1.25±0.15	0.78±0.10	0.03±0.11	20.689±0.116	0.104E-15±0.954E-18
59	21.87±0.07	21.18±0.02	20.59±0.10	19.43±0.09	18.52±0.10	18.48±0.13	0.70±0.07	0.59±0.10	1.16±0.14	0.91±0.14	0.04±0.16	22.767±0.053	0.835E-15±0.622E-17
60	20.27±0.06	19.92±0.02	19.36±0.13	18.25±0.07	17.46±0.09	17.42±0.10	0.35±0.06	0.56±0.13	1.11±0.15	0.79±0.11			

Table 4. continued

#	(1)	(2)	(3)	(4)	(5)	(6)	(7)	(8)	(9)	(10)	(11)	(12)	(13)	(14)
	B'	V	R	J	H	K'	$B-V$	$V-R$	$R-J$	$J-H$	$H-K'$	$R-K'$	$R(\text{knot})$	$F(H\alpha)$
71	20.77±0.06	20.35±0.02	19.83±0.12	18.63±0.07	17.64±0.09	17.57±0.08	0.42±0.07	0.52±0.12	1.19±0.14	0.89±0.11	0.07±0.12	21.329±0.095	—	—
72	20.07±0.06	19.64±0.02	19.11±0.14	17.99±0.08	16.89±0.09	16.80±0.08	0.42±0.07	0.53±0.14	1.13±0.16	1.09±0.12	0.09±0.12	20.993±0.098	—	—
73	22.16±0.13	21.27±0.07	20.70±0.10	19.96±0.52	19.56±0.54	19.13±0.78	0.88±0.15	0.58±0.13	0.72±0.63	0.41±0.75	0.43±0.95	20.984±0.085	—	—
74	20.34±0.07	19.92±0.02	19.36±0.13	18.26±0.10	17.21±0.10	17.15±0.12	0.42±0.07	0.56±0.14	1.10±0.17	1.05±0.14	0.06±0.15	21.364±0.083	—	0.818E-15±0.470E-17
75	20.89±0.07	20.38±0.03	19.81±0.12	18.70±0.14	17.66±0.11	17.80±0.19	0.51±0.07	0.56±0.13	1.11±0.17	1.04±0.18	-0.14±0.22	—	—	0.304E-15±0.182E-16
76	21.49±0.07	20.83±0.03	20.32±0.11	19.05±0.11	18.03±0.11	17.97±0.16	0.56±0.08	0.61±0.11	1.27±0.17	1.02±0.17	0.06±0.20	—	—	0.277E-15±0.996E-16
77	22.84±0.10	22.23±0.07	21.68±0.08	20.63±0.22	19.67±0.49	19.67±0.49	0.61±0.12	0.55±0.10	1.05±0.38	1.06±0.43	-0.11±0.54	—	—	0.122E-15±0.277E-17
78	23.01±0.10	22.29±0.06	21.74±0.08	21.22±0.55	19.56±0.19	19.39±0.33	0.72±0.12	0.55±0.10	0.52±0.55	1.66±0.58	0.17±0.38	—	—	0.133E-15±0.951E-18
79	22.42±0.14	21.96±0.13	21.64±0.09	20.38±0.70	—	—	0.46±0.19	0.32±0.15	1.25±0.71	—	—	—	—	0.514E-15±0.248E-17
80	20.52±0.07	20.11±0.03	19.64±0.13	18.66±0.18	17.61±0.13	17.95±0.30	0.41±0.08	0.47±0.13	0.98±0.22	1.05±0.22	-0.38±0.33	20.870±0.095	—	0.241E-14±0.326E-16
81	23.36±0.13	22.86±0.07	21.14±0.09	18.89±0.07	18.30±0.10	18.30±0.10	1.01±0.15	1.22±0.11	2.05±0.11	0.50±0.12	0.01±0.17	—	—	—
82	21.99±0.08	21.49±0.04	20.98±0.09	19.89±0.23	19.05±0.17	19.40±0.47	0.50±0.09	0.51±0.10	1.09±0.24	0.84±0.29	-0.38±0.50	22.511±0.060	—	—
83	21.46±0.11	—	20.19±0.11	18.78±0.25	17.87±0.37	17.90±0.37	—	—	1.41±0.28	0.91±0.31	-0.09±0.41	21.157±0.088	—	—
84	22.31±0.11	—	21.46±0.08	19.85±0.32	19.00±0.18	19.45±0.71	—	—	1.61±0.33	0.84±0.30	-0.43±0.75	—	—	—
85	22.10E-0.14	—	21.14E-0.09	19.92±0.60	19.71E-0.73	—	—	—	1.22E-0.61	0.22E-0.95	—	—	—	—

† Magnitudes and colors are not corrected for extinction

(1) Knot number (reverse DEC sorted)

(2) Johnson- B magnitude

(3) Johnson- V magnitude

(4) Johnson- R magnitude

(5) J magnitude

(6) H magnitude

(7) K' magnitude

(8) $B-V$

(9) $V-R$

(10) $R-J$

(11) $J-H$

(12) $H-K'$

(13) Johnson- R magnitude (underlying emission subtracted and not extinction corrected)

(14) $H\alpha$ flux (underlying emission subtracted and not extinction corrected) in $\text{erg s}^{-1} \text{cm}^{-2}$

Table 5. Emission-line fluxes

Knot	Slit	[OII] $\lambda 3727$	[NIII] $\lambda 3869$	H γ	[OIII] $\lambda 4363$	H β	[OIII] $\lambda 4959$	[OIII] $\lambda 5007$	[NII] $\lambda 5199$	H α $\lambda 6576$	[OI] $\lambda 6300$	H α	[NII] $\lambda 6583$	H α $\lambda 6678$	[SII] $\lambda 6716$	[SII] $\lambda 6731$	E(B-V)
14	6b	1.25E-15	—	—	2.47E-16	—	—	5.07E-16	—	—	—	—	—	—	—	—	—
16	3	3.17E-15	—	—	—	5.27E-16	5.38E-16	1.35E-15	—	—	—	—	—	—	—	—	—
19	4b	1.22E-14	—	—	—	6.08E-15	3.10E-15	1.01E-15	—	—	—	—	—	—	—	—	—
20*	4r	20*	—	—	—	6.08E-15	3.10E-15	1.01E-15	—	—	—	—	—	—	—	—	—
26*	1r	—	—	—	2.96E-15	3.66E-14	2.25E-14	1.12E-13	—	—	—	—	—	—	—	—	—
26*	2r	5.40E-14	3.86E-15	1.61E-14	1.57E-15	3.66E-14	2.25E-14	1.12E-13	—	—	—	—	—	—	—	—	—
26	1b	1.06E-13	6.77E-15	—	1.02E-15	3.80E-14	2.38E-14	7.05E-14	—	—	—	—	—	—	—	—	—
26*	2b	5.91E-14	1.99E-14	6.54E-14	2.78E-15	1.40E-13	7.56E-14	2.28E-13	—	—	—	—	—	—	—	—	—
26*	6b	4.62E-14	—	3.96E-14	7.18E-15	8.50E-14	4.20E-14	1.28E-13	—	—	—	—	—	—	—	—	—
27*	6r	—	—	—	—	1.94E-14	1.10E-14	3.35E-14	—	—	—	—	—	—	—	—	—
29	4b	4.88E-15	—	—	—	1.56E-16	1.19E-15	1.18E-15	—	—	—	—	—	—	—	—	—
32	2b	2.24E-14	6.18E-16	—	2.59E-16	8.40E-15	4.40E-15	1.32E-14	—	—	—	—	—	—	—	—	—
37*	5b	—	—	—	—	1.07E-15	5.57E-15	1.32E-14	—	—	—	—	—	—	—	—	—
37*	5b	—	—	—	—	1.42E-14	8.08E-15	1.12E-14	—	—	—	—	—	—	—	—	—
37*	6b	2.81E-14	—	6.62E-15	—	1.42E-14	2.05E-14	1.12E-14	—	—	—	—	—	—	—	—	—
37	3	—	—	3.31E-14	1.54E-14	7.11E-14	2.05E-14	6.31E-14	—	—	—	—	—	—	—	—	—
41	1b	4.16E-15	—	—	—	1.58E-15	7.48E-16	1.73E-15	—	—	—	—	—	—	—	—	—
42*	2r	1.67E-14	2.23E-15	—	—	8.08E-16	5.26E-15	1.05E-15	—	—	—	—	—	—	—	—	—
45*	1r	3.46E-15	—	—	—	8.87E-15	5.26E-15	1.60E-14	—	—	—	—	—	—	—	—	—
45	6r	—	—	—	—	7.43E-15	—	1.69E-14	—	—	—	—	—	—	—	—	—
45	4b	5.31E-15	—	—	—	1.00E-15	—	—	—	—	—	—	—	—	—	—	—
45	4b	4.12E-15	—	—	—	—	—	—	—	—	—	—	—	—	—	—	—
47*	6r	—	—	—	—	—	—	—	—	—	—	—	—	—	—	—	—
53*	2b	1.92E-14	—	2.05E-14	5.23E-16	1.97E-15	1.90E-14	2.72E-15	—	—	—	—	—	—	—	—	—
54*	4r	—	—	—	—	—	—	—	—	—	—	—	—	—	—	—	—
54	5r	3.13E-15	—	—	—	1.98E-16	—	—	—	—	—	—	—	—	—	—	—
54	5b	—	—	—	—	—	—	—	—	—	—	—	—	—	—	—	—
59	4r	6.03E-15	—	—	3.07E-16	1.34E-15	1.07E-15	7.20E-16	—	—	—	—	—	—	—	—	—
59	4b	—	—	—	—	3.19E-15	2.33E-15	2.89E-15	—	—	—	—	—	—	—	—	—
62*	1r	—	—	—	—	2.04E-15	5.63E-16	7.13E-15	—	—	—	—	—	—	—	—	—
62	3	—	—	—	—	9.76E-16	1.07E-15	1.25E-15	—	—	—	—	—	—	—	—	—
66*	5r	6.32E-15	5.44E-16	7.74E-16	1.10E-16	1.08E-15	6.98E-16	1.87E-15	—	—	—	—	—	—	—	—	—
66*	5b	6.65E-15	—	—	—	2.16E-15	4.69E-15	4.69E-15	—	—	—	—	—	—	—	—	—
66*	2b	7.69E-15	4.38E-15	5.06E-15	5.41E-16	1.09E-14	7.92E-15	5.26E-15	—	—	—	—	—	—	—	—	—
68*	2b	3.10E-15	2.10E-15	2.92E-15	6.24E-16	1.09E-14	7.92E-15	5.26E-15	—	—	—	—	—	—	—	—	—
70*	4r	8.44E-15	2.28E-14	2.13E-14	2.80E-15	4.57E-14	5.32E-15	1.80E-14	—	—	—	—	—	—	—	—	—
85	4b	—	—	—	—	2.45E-16	1.78E-16	5.66E-16	—	—	—	—	—	—	—	—	—

Fluxes in $\text{erg s}^{-1} \text{cm}^{-2}$

(see Appendix for a complete description). From the relation between the number of pixels and the threshold used we determine the physical size of the region at the e-folding of the equivalent two-dimensional Gaussian. The contours derived in this way will be not circular (see Fig. 2). This method avoids sistematic effects introduced in the contours and sizes determination due to changes in the underlying emission from one region to another.

The equivalent radii derived are given in Table 3 (Col. 5). Finally, this procedure allows to take into account the effect of the Point Spread Function (PSF hereafter) over the sizes derived. Thus, applying $\sigma^2 = \sigma_{\text{measured}}^2 - \sigma_{\text{seeing}}^2$, we obtain the radii corrected from the PSF effect (see Col. 6). The e-folding radius of the PSF in the H α and R-band images was $\sigma_{\text{seeing}} = 0''.72$. The radii at the e², e³-folding was, respectively, $\sqrt{2}$ and $\sqrt{3}$ times the e-folding radii derived.

4.3. Object classification

We have spectroscopic data for only 22 of the 85 regions detected in the neighborhood of Mrk 86 (see Table 5), 20 of them in the low resolution spectra and two, #18 and #40, in the high resolution ones. All these regions seem to belong to the galaxy, with heliocentric emission-lines velocities within the range 400 – 540 km s⁻¹ (see GZG). However, the nature of the remaining 63 objects is much more uncertain.

Fortunately, there are many other criteria that provide important clues about the nature of these objects, 1) if the host galaxy and some of these objects show line-emission (e.g., H α emission) within the wavelength range covered by a narrow-band filter ($FWHM \sim 50 - 100 \text{ \AA}$) they will probably have similar recession velocities within a range of $\Delta v \sim 1000 - 2000 \text{ km s}^{-1}$; 2) if one of these objects is placed in a high surface brightness region of the galaxy, and it has an extended morphology, it will probably belong to the host galaxy. On the other hand, regions that do not show line emission and 3) are placed in galaxy outer regions, or 4) show point-like morphology, should not be classified as belonging to the host galaxy.

In Table 3 we mark those regions identified spectroscopically as belonging to Mrk 86 with an **S** letter in Col. 8. Those regions showing photometric H α line-emission are marked with an **E** letter, and with an **N** those regions with extended morphology placed at short galactocentric distances. Extended objects placed at large galactocentric distances have been marked with a **B** (probably background galaxies). Finally, three point-like sources have been classified as F type (probably foreground stars; #4, #61 & #67).

It is worthwhile to check whether these point-like objects without emission lines belong to the galaxy. Their colors (see Sect. 6.2) indicate that objects #4, #61 and #67 are likely old type stars. Column 13 of Table 4 shows

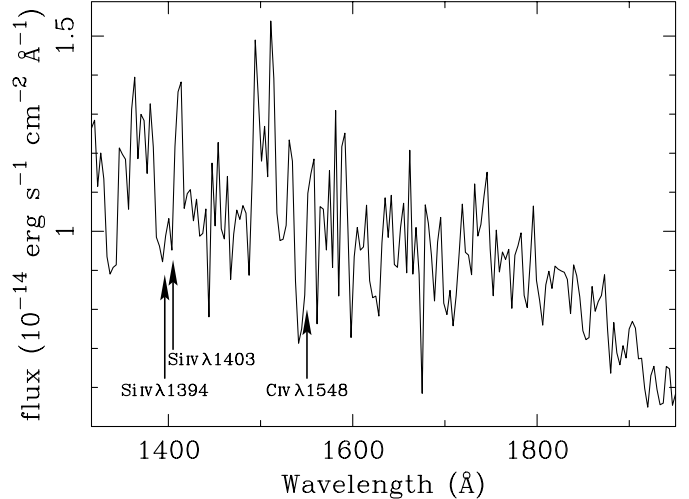


Fig. 4. IUE spectrum in the range 1150 – 1975 Å obtained with the SWP camera in the low dispersion mode. The spectrum has been smoothed using a 2 pixels boxcar filter. The Si IV λ 1394, 1403 Å and C IV λ 1548 Å spectral lines are shown with a clear P Cygni profile in the case of the C IV λ 1548 Å line

the R-band magnitudes of the regions after being subtracted from the galaxy background. Using a distance modulus of 29.2 we derive absolute magnitudes for these stars between 5 and 8 magnitudes too bright to belong to the galaxy. We conclude that objects #4, #61 and #67 are effectively foreground stars. In this work we will study only the **S**, **E** and **N** type objects.

4.4. Optical and nIR photometry

Using the contours obtained with COBRA, we have measured aperture $BVRJHK$ magnitudes and $B - V$, $V - R$, $R - J$, $J - H$, $J - K$ colors for all the regions in Table 4 (Cols. 2-7 for magnitudes, and 8-12 for colors). These apertures include both knot and underlying stellar population emission. Before measuring these colors we degraded the $BVRHK$ images to the worst seeing J-band image ($FWHM \sim 1.8''$). In addition, we measured integrated magnitudes in R-band for these regions, subtracted from the underlying emission as determined by COBRA (Table 4; Col. 13). Background subtracted H α fluxes were also measured and they are given in Table 4 (Col. 14). Due to the very bad seeing of the [O III] λ 5007 Å image we do not include photometric [O III] λ 5007 Å fluxes in our analysis.

The magnitudes and colors shown in Table 4 are measured quantities and they have not been corrected for extinction.

4.5. Optical spectroscopy

The relatively small slit width employed in these observations, prevents us from obtaining knot total emission

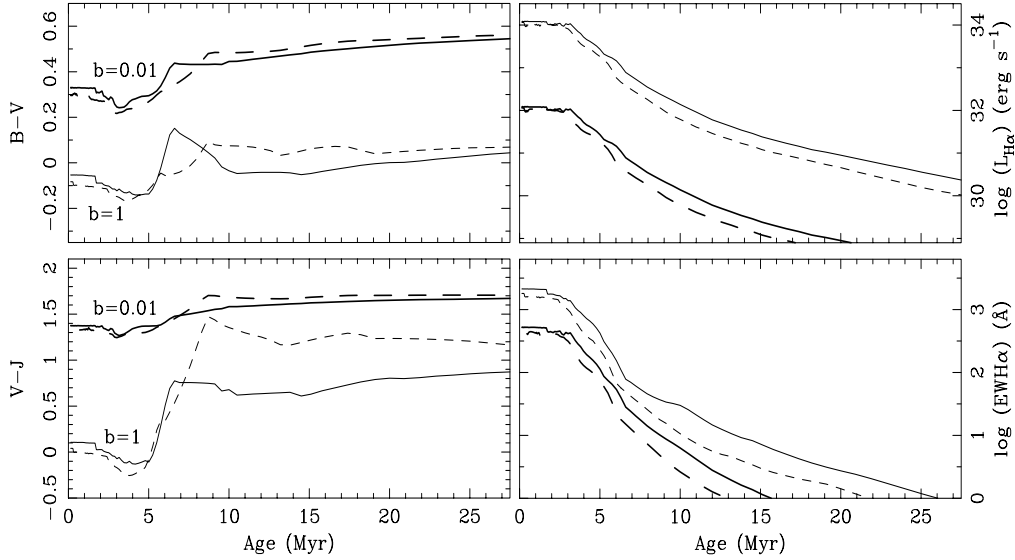


Fig. 5. Model predictions. The behavior of the evolutionary synthesis models is shown. We give the change in the $B - V$ and $V - J$ colors, $H\alpha$ luminosity and $H\alpha$ equivalent width for two different metallicities and burst strengths. *Solid-lines* represent models with two fifths solar metallicity, and *dashed-lines* represent solar metallicity models. *Thick-lines* are for $b = 0.01$ burst strength models and *thin-lines* are for pure burst models. These models have been computed assuming a fraction of 15 per cent of escaping Lyman photons

line fluxes. We will derive the emission line ratios in order to characterize the ionized gas properties in the galaxy star-forming regions. In Table 5 we give the line intensities measured in a region of $4''.30 \times 2''.65$ centered in the maximum of the emission knot section covered by the slit. These line intensities have been corrected for internal extinction when gas color excesses, $E(B - V)_{\text{gas}}$, were given. The $E(B - V)_{\text{gas}}$ values have been deduced from the $H\alpha - H\beta$ and $H\beta - H\gamma$ Balmer line ratios measured, and assuming the line ratios predicted for the recombination case-B by Osterbrock (1989). $H\beta$ line intensities have been measured deblending the absorption and emission components using the IRAF-STSDAS NGAUSSFIT task. The line intensities were measured separately in both b (blue) and r (red) spectra. When the line-ratios measured in both arms, typically $[\text{O III}]\lambda 5007/H\beta$, matched for a given region, we merged both data sets.

4.6. Ultraviolet spectroscopy

The aperture used in the UV spectra taken from the IUE Final Archive ($20'' \times 10''$) was centered in the brightest visual knot (#26) with position angle $\text{PA} = 117^\circ$. The UV spectra of this knot shows the strong absorption lines of $\text{Si IV}\lambda\lambda 1394, 1403 \text{ \AA}$ and $\text{C IV}\lambda 1548 \text{ \AA}$ (see Fig. 4). Although this spectrum has been smoothed, the signal-to-noise ratio prevents us from carrying out a quantitative analysis. However, this spectrum contains valuable information, showing a clear P Cygni profile on the $\text{C IV}\lambda 1548 \text{ \AA}$ line, typical of the fast and dense winds of O-type supergiants.

5. Evolutionary synthesis models

In order to derive the physical properties of the different stellar populations in Mrk 86 we have built a complete set of evolutionary synthesis models based in those developed by Bruzual & Charlot (priv. comm.).

First, we have assumed that the optical-near-infrared spectral energy distribution (SED) in any region of Mrk 86 can be described by a young star-forming burst superimposed on an underlying stellar population. The burst strength parameter, b , will describe the mass ratio between both stellar populations. Then, using this parameter and the evolution with time of the stellar continuum predicted by the Bruzual & Charlot (priv. comm.) models, we derive the colors and number of Lyman photons emitted for different composite stellar populations, with b ranging between 10^{-4} and 1. We have studied models with metallicities $1/50 Z_{\odot}$, $1/5 Z_{\odot}$, $2/5 Z_{\odot}$, Z_{\odot} and $2 Z_{\odot}$, and Scalo (1986) IMF with $M_{\text{low}} = 0.1 M_{\odot}$ and $M_{\text{up}} = 125 M_{\odot}$. The underlying population has been parametrized using the optical-near-infrared colours measured in the outer regions of Mrk 86. We use, $B - V = 0.69$, $V - R = 0.52$, $R - J = 1.27$, $J - H = 0.99$ and $R - K = 2.35$, as underlying stellar population colors, assuming that no significant color gradients are present (see Fig. 6). In addition, the mass-to-light ratio adopted for this stellar population in the K -band was $0.87 M_{\odot}/L_{K,\odot}$ (see Paper II).

Now, following the procedure described by Gil de Paz et al. (2000b) and Alonso-Herrero et al. (1996) we included the contribution to the total flux and

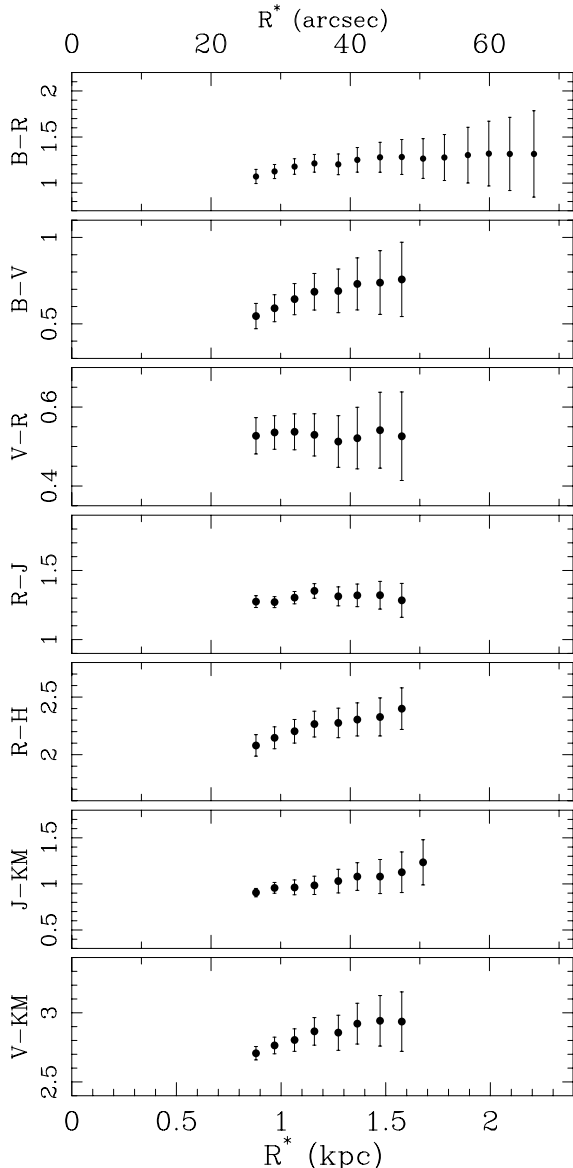


Fig. 6. Color profiles in the outer regions of Mrk 86

colors arising from the nebular continuum and the most intense emission-lines (i.e., $[\text{O II}]\lambda\lambda 3726, 3729 \text{ \AA}$, $\text{H}\beta$, $[\text{O III}]\lambda 4959 \text{ \AA}$, $[\text{O III}]\lambda 5007 \text{ \AA}$ and $\text{H}\alpha$, etc.).

We have assumed, in order to compute the nebular continuum emission, an electron density, n_e , of 10^2 cm^{-3} and a temperature, T_e , of 10^4 K . In addition, from the analysis of our spectroscopic data (see Paper II), we adopted a $N[\text{He II}]/N[\text{H II}]$ abundance ratio of 0.12. We have also assumed that the He III abundance is so low that the emission from recombination to He II is negligible.

Finally, we have included the contribution of the emission lines to the total flux. The contribution of the $\text{H}\beta$, $\text{H}\alpha$, $\text{Pa}\beta$, $\text{Br}_{10} - \text{Br}_{19}$ and $\text{Br}\gamma$ hydrogen emission lines to the $BVRJHK$ bands was obtained assuming the case-B of recombination (Osterbrock 1989) and using the relation given by Brocklehurst (1971). The

contribution of the most intense forbidden lines have been estimated using average $[\text{O II}]\lambda\lambda 3726, 3729/[\text{O III}]\lambda 5007$ and $[\text{O III}]\lambda 5007/\text{H}\beta$ line ratios, as provided by our spectroscopic data. Fortunately, the contribution of all the forbidden lines to the B and V bands is very small. Using the higher and lower line-ratios measured in the galaxy, this contribution would range between 1 and 8 per cent for the B -band and 2 and 8 per cent for the V -band, for a $\text{H}\alpha$ equivalent width (EW hereafter) of 100 \AA .

The output of the models will be the optical-near-infrared colors $B - V$, $V - R$, $V - J$, $J - H$ and $J - K$ of the composite stellar population, its $\text{H}\alpha$ luminosity and equivalent width, and mass-to-light ratio, parametrized as a function of the burst age, burst strength and stellar metallicity (t , b , Z).

The Cousins- R magnitudes originally given by the Bruzual & Charlot (priv. comm.) models have been converted to Johnson- R magnitudes using the relation given by Fernie (1983). However, if we compare the correction predicted by Fernie (1983) in the case of very red stars ($R_C - R_J \simeq 0.25^m$) with that measured by Fukugita et al. (1995) for early-type galaxies, typically of 0.1^m –with no correction for extinction applied–, we find differences of about 0.15^m . Since the change in $R_C - R_J$ due to the correction for extinction can not be higher than 0.02^m , this difference has to be attributed to a difference in the correction between evolved stellar populations and individual very-red stars. Thus, in the case of the underlying population analysis, we have applied the mean correction given by Fukugita et al. (1995).

6. Results

6.1. Underlying stellar population

The surface brightness profiles given in Fig. 3 show a clear exponential dominance at regions outer than $\sim 1.25 \text{ kpc}$. We have obtained the parameters of this exponential component on the deepest R -band profile yielding a scale, α , of $0.88 \pm 0.02 \text{ kpc}$ and an extrapolated central surface brightness, $\mu_{E,0}$, of $21.50 \pm 0.06 \text{ mag arcsec}^{-2}$. Papaderos et al. (1996a) obtained quite different values, $\alpha = 0.74 \pm 0.06 \text{ kpc}$ and $\mu_{E,0} = 19.42 \pm 0.03 \text{ mag arcsec}^{-2}$. This difference is not surprising considering that the R -band profile given Papaderos et al. (1996a) only reaches galactocentric distances of 2 kpc .

The color profiles in the galaxy outer regions, where the underlying stellar population dominates the total light profile, are shown in Fig. 6. No significant color gradients are observed at distances larger than $1.2 - 1.3 \text{ kpc}$, whereas at shorter distances a progressive and swallow blueing is derived. This blueing is probably related with an increment in the light contamination from high surface brightness star-forming regions associated to the *plateau* component. In Fig. 7 we show the $\text{H}\alpha$ profile compared with

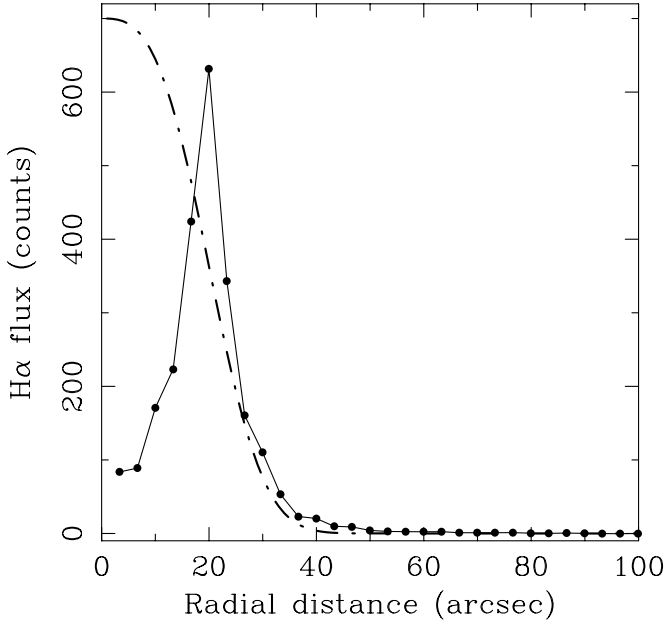


Fig. 7. $H\alpha$ profile obtained using the isophotes measured in the R -band image (*solid-line*). The surface brightness profile of the *plateau* component as parametrized by Papaderos et al. (1996a) in the B -band is also shown (*dot-dashed-line*)

the surface brightness profile in the B -band of the *plateau* component (see Papaderos et al. 1996a). From this figure it is quite clear that the progressive blueing observed at distances shorter than $40''$ is due to currently star-forming regions located in the *plateau* component.

6.2. Star-forming regions

In Sect. 4.3 we have classified the regions observed in the Mrk 86 neighborhood as **S**, **E**, **N**, **F** and **B** objects (**S**, spectroscopically confirmed; **E**, emission-line regions; **N**, extended and diffuse; **F**, foreground stars; **B**, background galaxies).

The optical-nIR colors measured for the **F** objects seem to indicate that the #4, #61 and #67 regions are, respectively, M0-M3, K2-K5 and G7-K0 spectral type foreground stars. Besides, between the **B** type objects (background galaxies), we find two very red objects, #2 and #3 regions, with $V-K$ colors of about 5 and 4^m , respectively.

Hereafter, we present the results for the study of the **S**, **E** and **N**-type regions. First, we have analyzed their R -band luminosities in Fig. 8a. We observe that this distribution has a clear maximum at $M_R = -9.5^m$. This distribution can not be well fitted using any standard power-law luminosity function (see, e.g. Elson & Fall 1985, for the LMC star-clusters LF).

In Fig. 8b we show the $H\alpha$ luminosity distribution of the galaxy emission-line regions. The $H\alpha$ luminosities used were corrected for internal extinction. In those cases where spectroscopic data were not available we used a mean color

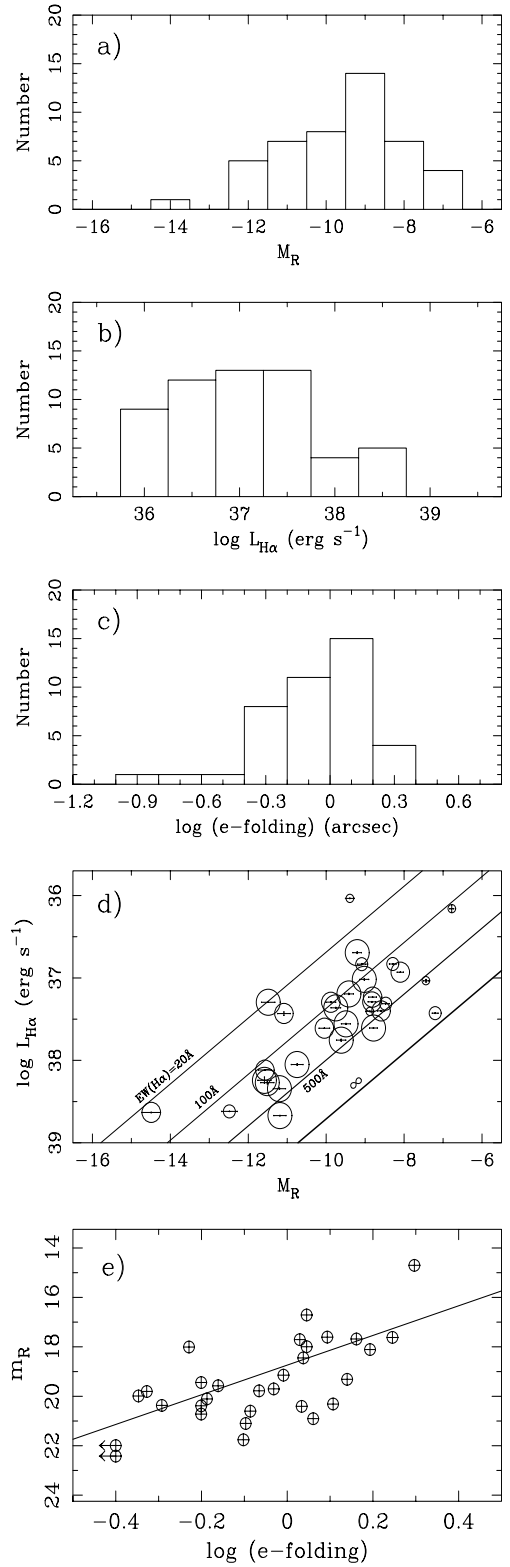


Fig. 8. a) R -band luminosity distribution for the **S**, **E** and **N**-type regions. b) $H\alpha$ luminosity distribution for the galaxy emission-line regions (**S** and **E** types). c) Radius distribution for the **S**, **E** and **N**-type regions. d) $H\alpha$ and continuum R -band luminosities comparison. Lines of constant $EW(H\alpha)$ are drawn. e) R -band apparent magnitude vs. radius

Table 6. Data for the Mrk 86 starburst component

Coordinates		
RA(J2000)	08 ^h 13 ^m 14.69 ^s	
DEC(J2000)	+45°59′21.9″	
Photometry		
$B - V$	0.39 ± 0.06	
$V - R$	0.54 ± 0.25	
$V - J$	1.59 ± 0.02	
$J - H$	0.77 ± 0.08	
$J - K'$	0.85 ± 0.03	
M_R	-14.0 ± 0.2	
Radius	4.3″	
Spectroscopic indexes		
Slit	#4b	#1b
D_{4000}	1.38	1.38
Mg2	0.06	0.04
H δ^\dagger	6.0 Å	6.2 Å
Fe5270	1.20 Å	–
Fe5406	0.74 Å	–
Region	21″45 × 2″65	14″3 × 2″65

[†] Equivalent width in absorption.

excess of $E(B - V)_{\text{gas}} = 0.34^{\text{m}}$. The distribution obtained is nearly flat in the luminosity range $10^{37.7} - 10^{38.7} \text{ erg s}^{-1}$, with most of the H II regions showing H α luminosities in the range $10^{36} - 10^{39} \text{ erg s}^{-1}$. This luminosity range corresponds to star formation rates between $6 \cdot 10^{-5}$ and $0.06 M_{\odot} \text{ yr}^{-1}$ (Gil de Paz et al. 2000b). The spatial resolution of the H α image is about 40 pc. Therefore, the scarcity of H II regions fainter than $10^{36} \text{ erg s}^{-1}$ can not be explained as an effect of the spatial resolution (see Kennicutt et al. 1989).

It should be noticed that some of these H α emitting regions showing very faint or null continuum emission (#7, #9, #12, #50), seem to be pure gas regions photoionized by distant stellar clusters. These regions are in many cases associated with the rim of expanding bubbles (see Martin 1998, GZG).

Now, in Fig. 8c we show the radius distribution measured in the R -band image (given by the e-folding radius; see Appendix). These radii have been corrected for the PSF contribution (see Sect. 4.2). This distribution shows a maximum at about 1 arcsec, that corresponds to a $FWHM$ of about 55 pc.

In Fig. 8d, the R -band and H α luminosities are compared. The lines drawn suggest that these regions have equivalent widths of H α ranging between 100 – 500 Å. Since both, H α and R -band fluxes have been measured subtracted from the contribution of the underlying population, these $EW(\text{H}\alpha)$ are pure H II region equivalent widths. In this figure the symbol size is proportional to the extinction corrected $B - V$ color, using larger symbols for bluer regions. Finally, we have compared (see Fig. 8e) the knot apparent magnitude and the physical radius, both measured on the R -band image using the

COBRA program. If all these star-forming regions were optically thin at these wavelengths and they had similar star densities we would expect the flux to be proportional to the cube of the radius. In Fig. 8e the best fit to the function $F_R \propto R^3$ is also shown.

6.3. Central starburst

Finally, we have studied the region classified by Papaderos et al. (1996a) as the starburst component (see Fig. 2). This component appears as a bright, extended and not very well defined region in the broad-band $BVRJHK$ images (see Fig. 1).

The integrated blue color measured by Papaderos et al. (1996a) in the galaxy central parts, $B - R \simeq 0.9$ (0.93 ± 0.26 in our work), similar to that observed in Scd and Im galaxy types (Fukugita et al. 1995), indicates the existence of a young stellar population superimposed on the evolved underlying component. However, the absence of significant gas emission (see the H α image in Fig. 1) suggests an intermediate aged dominating population. In Table 6 we give the colors and spectroscopic indexes measured for this region (see Trager et al. 1998) at two different slit positions⁴. The integrated optical-near-infrared colors shown in Table 6 have been measured on the R -band image using an aperture with radius 4.3″ (1 e-folding), as given by the COBRA program. This aperture is marked in Fig. 2 with a *thick-lined* contour. These colors have not been corrected for extinction. The M_R absolute magnitude has been measured subtracted from underlying emission. The spectroscopic indexes have been measured in the integrated spectra of the starburst section covered by the slits #4b and #1b. (see Table 2; see also Fig. 1 of GZG).

In Paper II we will derive the physical properties of this region by comparing the optical-nIR colors obtained with the predictions of our evolutionary synthesis models. In addition, the spectroscopic indexes measured will be compared with those predicted by the Bruzual & Charlot (priv. comm.) evolutionary synthesis models.

7. Conclusions

In this paper, the first of two, we have presented the observations and data analysis for the optical-near-infrared study of the Blue Compact Dwarf galaxy Mrk 86. We have taken $BVRJHK$, H α and [O III] λ 5007 Å images and long-slit optical spectroscopy for the object. Thus, using all these data,

- we have obtained the underlying population surface brightness and color profiles. The deepest R -band image yields an exponential profile for this component

⁴ The spectroscopic indexes have been measured using the REDUCEME package (Cardiel et al. 1998).

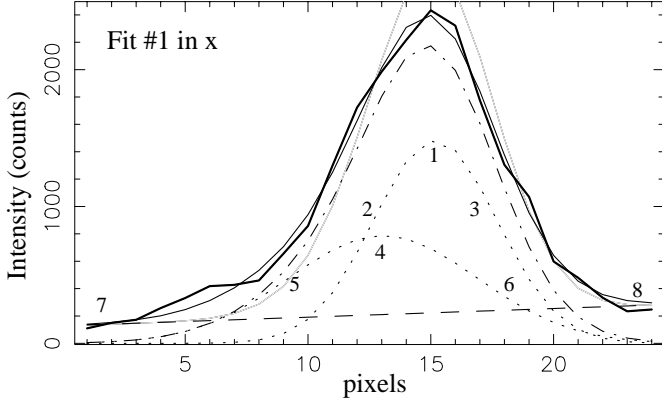


Fig. 9. Example of an observed x -axis light profile (*thick solid-line*) and its corresponding best fit (*thin solid-line*). The *dotted-lines* correspond to the two Gaussian components, being the *dot-dashed-line* the sum of these two components. The underlying emission (background) is represented by the *dashed-line*. The approximate positions for the 8 points used for defining the initial set of parameters are also shown. The spatial scale of the image was $0''.333 \text{ pixel}^{-1}$

with extrapolated central surface brightness of $\mu_{E,0} = 21.5 \text{ mag arcsec}^{-2}$ and scale, $\alpha = 0.88 \text{ kpc}$. No significant color gradients are observed in this component at distances larger $1.2 - 1.3 \text{ kpc}$;

- we have cataloged and classified all the regions observed in the neighborhood of the galaxy. If these regions are associated with the galaxy have been classified as **S** (spectroscopically confirmed), **E** (confirmed by their photometric $H\alpha$ or $[\text{O III}]\lambda 5007 \text{ \AA}$ emission) or **N** (diffuse and placed in the galaxy central region) type regions. **S** and **E** type objects are accepted to be galactic H II regions. **N** objects are, probably, evolved stellar clusters, with negligible Lyman continuum emission. On the other hand, background galaxies and foreground stars are classified as **B** and **F** types, respectively;
- we have also described the set of evolutionary synthesis models used in Paper II. These models are based in those developed by Bruzual & Charlot (priv. comm.). They have been obtained for metallicities between $1/50 Z_{\odot}$ and $2 Z_{\odot}$, and burst strength ranging between 10^{-4} and 1. We have included nebular continuum and recombination and forbidden lines emission. Although the contribution of the forbidden-line fluxes is quite uncertain in those regions where spectroscopic data are not available, the contribution of these lines in the $RJHK$ bands is negligible and lower than 8 per cent for the BV -bands (assuming an $EW(H\alpha) \sim 100 \text{ \AA}$);
- the optical-near-infrared colors, fluxes, emission line intensities of the **S**, **E** and **N** regions have been measured. Optical and near-infrared colors have been measured. The physical properties of the galaxy star-forming regions will be derived in Paper II,

comparing these data with the evolutionary synthesis models developed. This comparison will be performed using a method based in the combination of Monte Carlo simulations, a maximum likelihood estimator, a single linkage clustering analysis method and the Principal Component Analysis (PCA);

- finally, we provide optical-near-infrared colors and spectroscopic indexes for the central starburst component.

Appendix A: COBRA program

Due to the large number of star-forming regions in Mrk 86 and the intense and variable underlying emission we developed a program that allowed us to subtract this underlying emission and the occasional contamination from neighbor star-forming regions. Then, on the underlying emission subtracted image, we determined the most reliable apertures, sizes, and integrated fluxes for all these regions. This program was written in FORTRAN77 programming language and it was called COBRA (see <http://www.ucm.es/info/Astrof/cobra/>).

COBRA uses different graphic output devices, including XWINDOWS and Postscript, and makes use of the AMOEBA (Press et al. 1986), PGPLOT, FITSIO and BUTTON (Cardiel et al. 1998; see also Cardiel 1999) sub-routines.

In this Appendix we will describe the procedure followed to estimate the underlying emission and the criteria used to determine the sizes and fluxes of the star-forming regions and stellar clusters in Mrk 86 using the program COBRA.

A.1. Light profiles fitting

First, (1) an image section including the region of interest is selected interactively (see the original images in Fig. 10). The size of this section necessarily depends on the spatial scale of the change in the underlying emission and the proximity of neighbor regions. This section must be chosen in such a way that the background emission (underlying and neighbor regions emission) can be reproduced by a line in the x and y light profiles. Thus, when several relative maxima are placed too close to match this criterion they were studied as a single region.

After cropping the image section selected, (2) the position of the maximum of the region of interest is marked interactively. Then, the light profile along the x axis at this position is fitted.

In order to perform this fit three different components are used, a line that reproduced the underlying and neighbor regions contamination and two Gaussians that allowed to reproduce the light profile of the region of interest. In principle, any smooth, monotonic light profile can be approximated by a serie of Gaussians (somewhat analogous

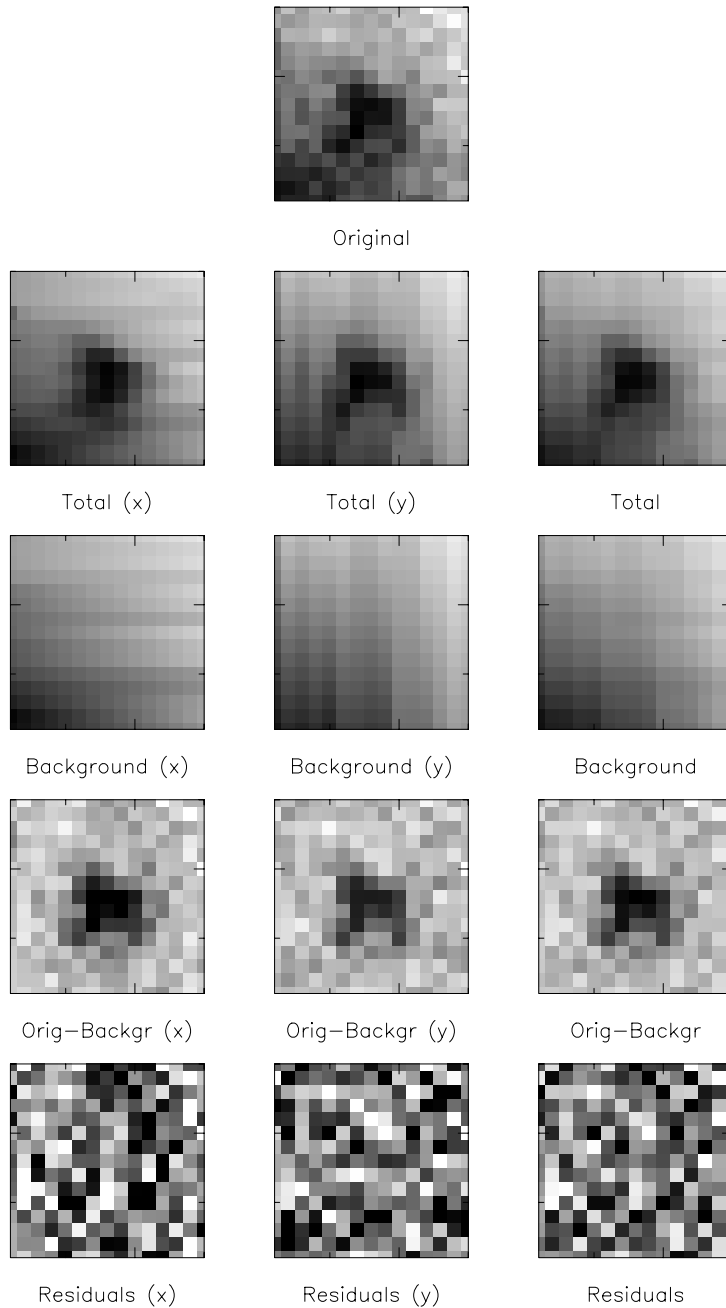


Fig. 10. Original, total (reconstructed), background, original minus background model and residuals images in both axis and the average as obtained for the region #6 in the *R*-band. The cuts in the original, total and background images are the same and equal to the maximum and minimum value in the original image. The cuts in the residuals images correspond to plus/minus one tenth the difference between the maximum and minimum in the background averaged image. The residuals images were obtained as the original image minus the total (reconstructed) image

to the Fourier series), not only the PSF of an image, but also the light profiles of remote stellar clusters or galactic cores (see Bendinelli et al. 1990). Two Gaussians are employed in order to reproduce the light profile of these regions because the use of a larger number of components led in some cases to solutions with no physical meaning.

Then, the best fit for the initial light profile using the minimization subroutine AMOEBA is obtained. The AMOEBA subroutine needs an initial set of solutions which can be defined by the 8 parameters of the function to minimize (3 for each Gaussian and 2 for the line). These parameters were introduced interactively marking

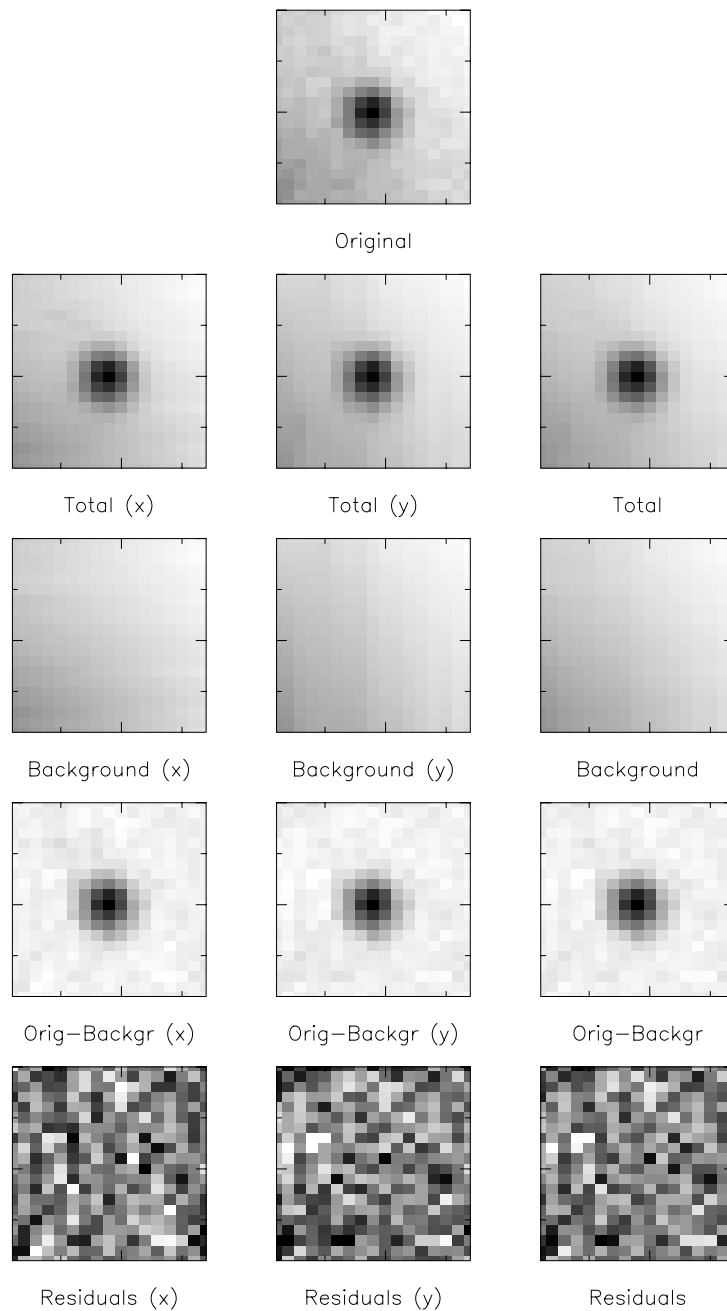


Fig. 10. continued (region #11)

the approximate position of the center and $FWHM$ for each Gaussian and two extreme values in the profile for the line. In Fig. 9 we show an example of the positions of the points used to define the set of initial parameters for the fit. Points 1, 2, 3 and 4, 5, 6 led to the initial parameters for the two Gaussians and points 7, 8 for the line. Using this set of parameters, (3) the best-fitting light profile is obtained (see Fig. 9).

Then, from the output of this fit and introducing the new positions of the two Gaussian maxima, (4) all the x axis profiles are fitted starting from those profiles adjacent to the initial one. The need of using previous results for the subsequent fits constitutes the main reason for starting this fitting procedure at the maximum of the emission region.

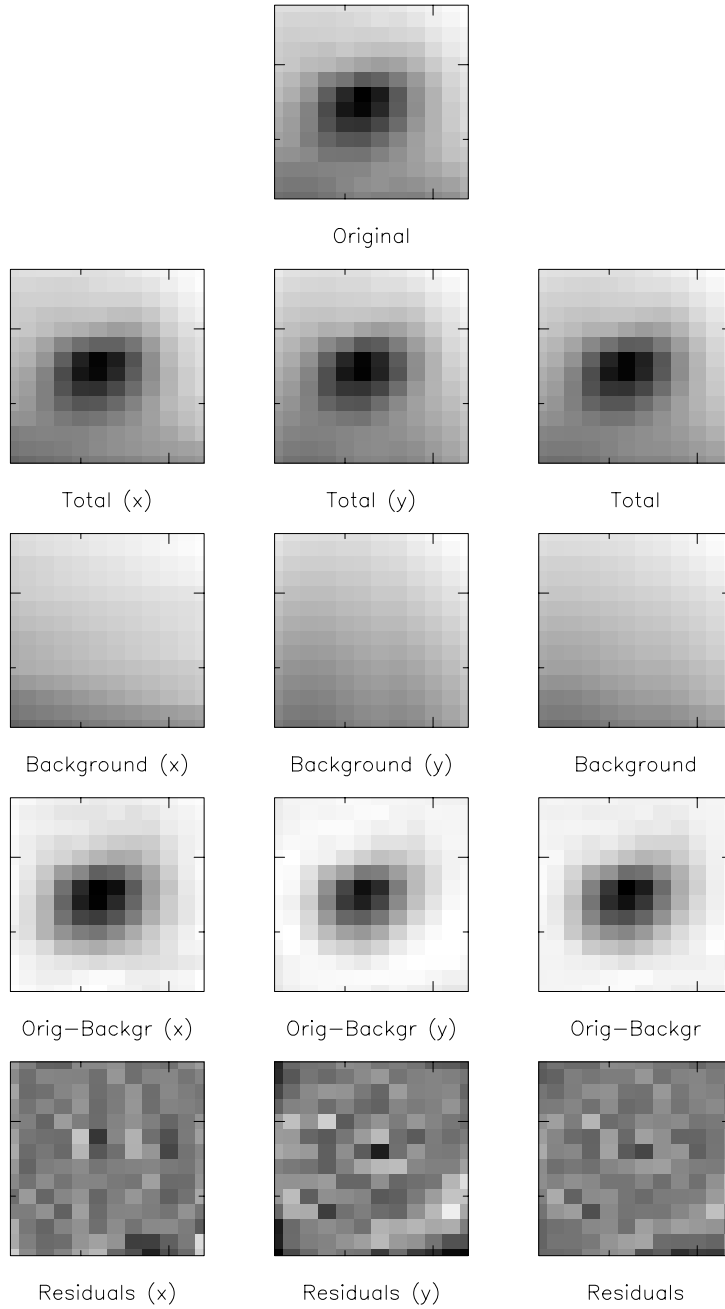


Fig. 10. continued (region #18)

Next, (5) the same fitting procedure is applied to the y axis profiles. Finally, after the profiles have been fitted in both axis, the underlying emission images reconstructed are averaged and subtracted from the original input image (see several examples in Fig. 10). This background-free image is then used to determine the centers, apertures, sizes and integrated fluxes of the different regions.

A.2. Position, sizes and fluxes

The knot center is taken as the maximum of the sum of the two Gaussian components. Then, computing the knot surface, A_x , above different thresholds, I_x , we can estimate the equivalent knot e-folding radius, $R_{e\text{-folding}}$, using,

$$R_{e\text{-folding}} = \sqrt{\frac{A_x}{\pi \ln\left(\frac{I_{\max}}{I_x}\right)}} \quad (1)$$

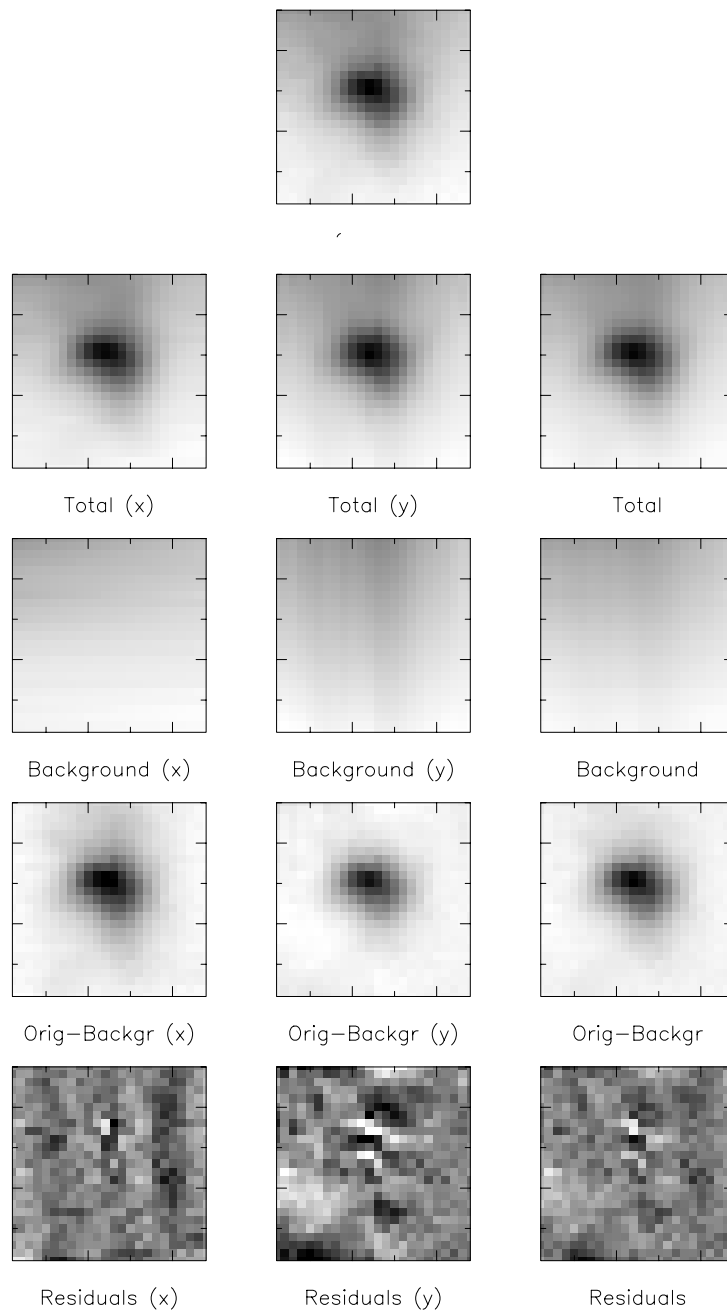


Fig. 10. continued (region #70)

where I_{\max} is the knot maximum intensity. In Fig. 11 we show the change in the area A_x for different thresholds as measured in the background subtracted image of the star-forming region #18 (with 1 e-folding radius of $0''.93$). The relatively small change deduced for the e-folding radius with the threshold guarantees the goodness of this size determination procedure.

The e^2 and e^3 -folding radii are then computed as $\sqrt{2}$ and $\sqrt{3}$ times the e-folding radius. Then, the knot contours are derived at these three radii, i.e. at $I_{\max}/I_x = e$,

e^2 , e^3 . The knot total flux is computed as the total flux in the background subtracted image. In order to ensure that most of the knot flux was included we derive the knot growing-curve, finding differences not larger than 20 per cent between total and growing-curve extrapolated flux.

Acknowledgements. Based on observations at the Jacobus Kapteyn, Isaac Newton and William Herschel telescopes operated on the island of La Palma by the Royal Greenwich Observatory in the Spanish Observatorio del Roque de los

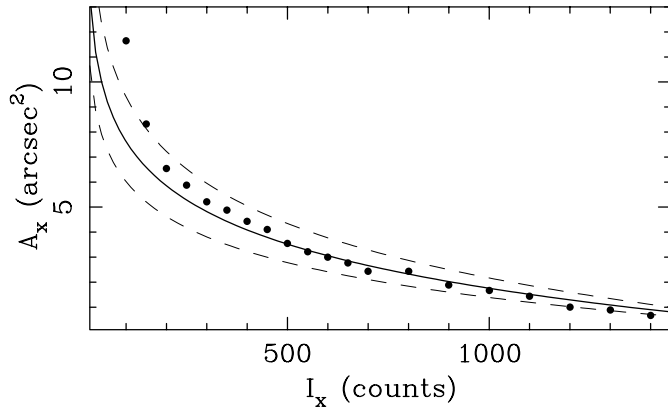


Fig. 11. Change in the area (A_x) of the region #18 with the threshold, I_x . The *solid-line* represents the result expected for a radius of 0.9 at 1 e-folding. The *dashed-lines* correspond to 0.8 and 1.0 e-folding radii

Muchachos of the Instituto Astrofísico de Canarias and from *International Ultraviolet Explorer* archive at the ESA VILSPA observatory. Based also on observations collected at the German-Spanish Astronomical Center, Calar Alto, Spain, operated by the Max-Planck-Institut für Astronomie (MPIA), Heidelberg, jointly with the Spanish “Comisión Nacional de Astronomía”.

We are grateful to Carme Jordi and D. Galadí for obtaining the *V*-band image. We would like to thank C. Sánchez Contreras and L.F. Miranda for obtaining the high resolution spectra, N. Cardiel for providing the REDUCEME package and C.E. García Dabó for the PLATEASTROM routine. We also thank A. Alonso-Herrero for her help in the acquisition and reduction of the nIR images. We also acknowledge Dr. Tosi for several helpful comments. Finally, we thank to C.E. García Dabó and J. Cenarro for stimulating conversations, and M. Sharina for providing a reprint copy of her article. This research has been supported in part by the grants PB93-456 and PB96-0610 from the Spanish “Programa Sectorial de Promoción del Conocimiento”. A. Gil de Paz acknowledges the receipt of a “Formación del Profesorado Universitario” fellowship from the Spanish “Ministerio de Educación y Cultura”.

References

- Alonso-Herrero A., Aragón-Salamanca A., Zamorano J., Rego M., 1996, *MNRAS* 278, 417
- Aragón-Salamanca A., Ellis R.S., Couch W.J., Carter D., 1993, *MNRAS* 262, 764
- Arp H., 1966, *Atlas of Peculiar Galaxies*. California Institute of Technology, Pasadena
- Bandinelli O., Parmeggiani G., Zavatti F., Djorgovski S., 1990, *AJ* 99, 774
- Bonatto C., Bica E., Pastoriza M.G., Alloin D., 1999, *A&A* 343, 100
- Bottinelli L., Gouguenheim L., Fouqué P., Paturel G., 1990, *A&AS* 82, 391
- Brocklehurst M., 1971, *MNRAS* 153, 471
- Burkert A., 1989, Ph.D. Thesis, Munich
- Campbell A.W., Terlevich R., 1984, *MNRAS* 211, 15
- Cardiel N., 1999, Ph.D. Thesis, Universidad Complutense de Madrid
- Cardiel N., Gorgas J., Cenarro J., González J.J., 1998, *A&AS* 127, 597
- Cassatella A., Barbero J., Benvenuti P., 1985, *A&A* 144, 335
- Doublier V., 1998, Ph.D. Thesis, Marsella
- Drinkwater M., Hardy E., 1991, *AJ* 101, 94
- Dultzin-Hacyan D., Masegosa J., Moles M., 1990, *A&A* 238, 28
- Elias J.H., Frogel J.A., Matthews K., Neugebauer G., 1982, *AJ* 87, 1029
- Elson R.A.W., Fall S.M., 1985, *PASP* 97, 692
- Fanelli M.N., O’Connell R.W., Thuan T.X., 1988, *ApJ* 334, 665
- Fernie J.D., 1983, *PASP* 95, 782
- Fuentes-Masip O., 1997, Ph.D. Thesis, La Laguna
- Fukuguita M., Shimasaku K., Ichikawa T., 1995, *PASP* 107, 945
- García-Dabó C.E., Gallego J., 1999, *Ap&SS* 263, 1-4
- Gil de Paz A., Zamorano J., Gallego J., 1999, *MNRAS* 306, 975 (GZG)
- Gil de Paz A., Zamorano J., Gallego J., 2000a, *A&A* (Paper II)
- Gil de Paz A., Aragón-Salamanca A., Gallego J., et al., 2000b, *MNRAS* 316, 357
- Giovanelli R., Haynes M.P., Herter T., et al., 1997, *AJ* 113, 53
- Hoffman G.L., Salpeter E.E., Helou G., 1990, in the proceedings of the Edwin Hubble Centennial Symposium, p. 67
- Kennicutt R.C., Edgar B.K., Hodge P.W., 1989, *ApJ* 337, 761
- Kent S.M., 1985, *PASP* 97, 165
- Klein U., Wielebinski R., Thuan T.X., 1984, *A&A* 141, 241
- Klein U., Weiland H., Brinks E., 1991, *A&A* 246, 323
- Kunth D., Sargent W.L.W., 1986, *ApJ* 300, 496
- Kunth D., Maurogordato S., Vigroux L., 1988, *A&A* 204, 10
- Landolt A.U., 1973, *AJ* 78, 959
- Loose H.-H., Thuan T.X., 1985, *The Morphology and Structure of BCDGs from CCD Observations*, in: *Star-Forming Dwarf Galaxies*. Kunth D., Thuan T.X., and Van J.T.T. (eds.). Éditions Frontières
- Markarian B.E., 1969, *Astrofizika* 5, 443
- Marlowe A.T., Heckman T.M., Wyse R.F.G., Schommer R., 1995, *ApJ* 438, 563
- Martin C.L., 1998, *ApJ* 506, 222
- Mazzarella J.M., Boroson T., 1993, *ApJS* 85, 27
- Norton S., Salzer J.J., 1997, *BAAS* 190
- Osterbrock D.E., 1989, *Astrophysics of Gaseous Nebulae and Active Galactic Nuclei*. University Science Books, Mill Valley, California
- Papaderos P., Loose H.-H., Thuan T.X., Fricke K.J., 1996a, *A&AS* 120, 207
- Papaderos P., Loose H.-H., Fricke K.J., Thuan T.X., 1996b, *A&A* 314, 59
- Petrosian A.R., Boulesteix J., Comte G., Kunth D., LeCoarer E., 1997, *A&A* 318, 390
- Press W.H., Flannery B.P., Teukolsky S.A., Vetterling W.T., 1986, *Numerical Recipes*. Cambridge University Press
- Rood H.J., Dickel J.R., 1976, *ApJ* 205, 346
- Sage L.J., Salzer J.J., Loose H.-H., Henkel C., 1992, *A&A* 265, 19
- Scalo J.M., 1986, *Fund. Cosmic Phys.* 11, 1
- Searle L., Sargent W.L.W., 1972, *ApJ* 173, 25
- Searle L., Sargent W.L.W., Bagnuolo W.G., 1973, *ApJ* 179, 427

- Shapley H., Ames A., 1932, *Ann. Harvard College Obs.* 88, No. 2
- Sharina M.E., Karachentsev I.D., Tikhonov N.A., 1999, *Astron. Lett.* 25, 322
- Silk J., Wyse R.F.G., Shields G.A., 1987, *ApJ* 322, L59
- Thronson Jr. H.A., Telesco C.M., 1986, *ApJ* 311, 98
- Thuan T.X., 1983, *ApJ* 268, 667
- Thuan T.X., 1991, *Observations and Models of Blue Compact Dwarf Galaxies*, in: *Massive Stars in Starbursts*, Leitherer C., Walborn R.N., Heckman T.M., Norman C.A. (eds.). Cambridge University Press, p. 183
- Thuan T.X., Martin G.E., 1981, *ApJ* 247, 823
- Trager S.C., Worthey G., Faber S.M., Burstein D., González J.J., 1998, *ApJS* 116, 1
- Verter F., 1985, *ApJS* 57, 261
- Wainscoat R.J., Cowie L.L., 1992, *AJ* 103, 332